



A DISCUSSION OF PAST AND ONGOING WORK

# On the Design and Control of Highly Backdrivable Lower-Limb Exoskeletons

GE LV, HANQI ZHU, and ROBERT D. GREGG

Digital Object Identifier 10.1109/MCS.2018.2866605

Date of publication: 13 November 2018



**L**ower-limb exoskeletons are external mechanical structures that support and assist human users during locomotion. The earliest studies on exoskeletons date back to the 1960s, whereas, over the previous decade, research on powered lower-limb exoskeletons has substantially expanded [1]. Exoskeletons with different architectures have been developed to achieve various goals. Typically, lower-limb exoskeletons can be classified into two broad categories based on their intended use: assisting people who have pathological gaits and augmenting able-bodied users. The first type of exoskeleton is designed to aid individuals with neurological conditions, for example, stroke or spinal cord injury (SCI). With the help of an exoskeleton, these people can complete different tasks that they cannot complete without assistance. For example, the bilateral hip-knee exoskeletons ReWalk [2] and Ekso Bionics [3] enforce predefined reference trajectories determined by a finite-state-machine structure to assist individuals with SCI. The bilateral Wandercraft exoskeleton adopts a hybrid dynamics-based controller to stabilize dynamically feasible periodic gaits for users with SCI, while allowing them to actively control the exoskeleton speed through upper-body posture [4].

The second type of exoskeleton is mainly used by able-bodied users for carrying heavy gear and operating cumbersome tools. The majority of these devices transmit force to the ground while tracking a desired reference torque. The Berkeley Lower Extremity Exoskeleton allows soldiers to carry heavy loads by using its actuators to minimize the interaction forces between the device and the user [5]. The Sarcos-Raytheon XOS exoskeleton and the Human Universal Load Carrier exoskeletons are also military-based devices aimed at soldier performance enhancement [1]. The soft exosuits presented in [6] can reduce the net metabolic rate for able-bodied subjects during walking by generating assistance through an offboard actuation system and Bowden cables. With advancements in hardware and microcontroller design, an increasing number of complex control algorithms are being realized in practice to promote the rapid development of powered lower-limb exoskeletons.

The majority of assistive exoskeletons are designed to rigidly track time-based kinematic patterns, which forces

users to follow specific joint positions during walking. The ReWalk and Ekso Bionics exoskeletons (as well as other devices [7]–[12]) employ high-ratio transmissions (for example, ball screws or harmonic drives) to achieve the high torques required to track lower-limb kinematics. These rigid actuators are ideal for position-based control methods as human torques or external force perturbations cannot easily rotate these actuators. Although these systems have shown promising results in assisting individuals with SCI, their kinematic control approaches are limited to replicating the normative joint kinematics associated with one specific task and user at a time [1]. These predefined trajectories cannot adjust to continuously varying activities or changes in user behavior associated with learning during gait rehabilitation. This control approach must also recognize the user's intent to transition from one task-specific controller to another [2], [13], which is hard to realize in practice [14]. Multiple task-specific controllers also require more tuning time for each user [15], [16]. Moreover, rigid position control methods require little or no contribution from the human user [17]. This may make sense for people with SCI, but it does not for individuals who have partial or full volitional control of their limbs. For example, poststroke individuals should be allowed to adjust their joint kinematics during the learning process based on corrections from the therapist. Unfortunately, high-ratio transmissions have high mechanical impedance, which prevents users from moving their joints freely without help from the exoskeleton. Individuals with volitional control of their lower extremities require novel design and control methods for exoskeletons that are more compatible with human interaction.

A necessary requirement for assisting or augmenting volitional human motion is for the exoskeleton joints to have low mechanical impedance (that is, be backdrivable or mechanically transparent). An exoskeleton is said to be backdrivable if users can drive their joints without a high-resistive torque from the exoskeleton. This has been achieved in various ways in the past. Active force control attempts to zero the interaction forces measured by a load cell to make the exoskeleton move with the human [5]. However, this approach has limited bandwidth that prevents more dynamic motions and cannot absorb impact forces [18], [19]. Although the Indego exoskeleton was originally designed for persons with SCI [20], its backdrivable electromechanical actuators have facilitated experiments with poststroke individuals by providing gravity compensation to the swing leg and user/task-specific feedforward movement assistance [13]. The powered knee orthosis in [21] uses a hydraulic actuator to achieve great backdrivability without sacrificing output torque. However, electric motors tend to be several times more efficient than hydraulic actuators [18], [22]. Devices with series elastic actuators can realize active backdrivability by servoing the spring displacement to zero. However, major limitations still exist,

such as low output torque [23], [24], complex system architecture [25], [26], and limited force/torque control bandwidth [24], [27]. Soft exosuits [28] by design have low joint impedance, but the control problem becomes substantially more difficult, due to uncertainty in the actuation model from transferring forces to the body through soft, compliant material (rather than a rigid structure). Recently, the field of legged robots has started embracing direct-drive and quasi-direct-drive actuation systems (for example, [18], [19], and [29]) to enable low-impedance actuation for highly dynamic motions, compliance to impacts, and accurate torque control. We propose that this design philosophy can also be applied in rehabilitation robots to provide users with a cooperative human-machine interface. Having low-impedance actuation also allows the implementation of novel human-interactive control strategies, making it possible to promote user participation and thus broaden the scope of application for these devices.

Low-impedance actuation is necessary but not sufficient for designing human-interactive exoskeletons because traditional kinematic control methods can still command large torques that interfere with the volitional motion of the human. Traditional high-gain position control strategies actively increase the overall impedance of the human and

exoskeleton system in closed loop, defeating the purpose of the low-impedance actuator design. Therefore, the final requirement concerns the control strategy, which must aid without overly constraining the user's joint kinematics. Instead of tracking reference kinematic patterns, kinetic goals (for example, energy or force) can be enforced to provide a flexible learning environment and allow users to choose their own kinematic patterns.

In addition to training flexibility, the control method should be task-invariant to provide consistent assistance that eliminates the need for detecting task transitions. Although some task-invariant controllers have been proposed for amplifying human motion [5], [30] or compensating for exoskeleton mass/inertia [13], [31], these approaches assume that the user has the ability to produce the joint kinematics, which is not the case with weakened limbs. Therefore, we focus on an energetic control approach that shapes the Lagrangian [that is, kinetic energy (KE) minus potential energy (PE)] of the human body and exoskeleton in closed loop. This energetic control approach, known as *energy shaping*, controls the system energy to a specific analytical function of the system state to induce different dynamics via the Euler–Lagrange equations [32]. By shaping PE, torques can be generated to counteract gravity in the vertical direction. This control action yields so-called body-weight support (BWS), which offloads the perceived weight of the user's lower extremities and center of mass (COM). Similarly, KE shaping can reduce the perceived mass and inertia of the human-robot system to generate assistance in all directions of motion. Because this control method augments the joint dynamics rather than tracking joint kinematics, the exoskeleton determines how the joints should move instead of where they move. Therefore, the assistance is invariant of the task and the preferred kinematics of the user.

As discussed in "Summary," this article summarizes our previous and ongoing work to demonstrate the design and control philosophy behind task-invariant exoskeletal assistance. The proposed design philosophy was applied to build a powered ankle exoskeleton (Generation Zero) that served as a tethered engineering testbed for preliminary experiments [33]. The design of a mobile-powered knee-ankle exoskeleton (Generation One) using a high torque-density electrical motor and a custom low-ratio transmission was then presented [34], which can achieve high-torque output without sacrificing intrinsic backdrivability or efficiency. To control these exoskeletons in a human-cooperative manner, we propose a complete theoretical framework for underactuated energy shaping that incorporates both environmental and human interaction [35]–[37]. By explicitly modeling holonomic contact constraints in the dynamics, we transform the conventional Lagrangian dynamics into the equivalent constrained dynamics (ECDs) that have fewer (or possibly zero) unactuated degrees of freedom (DOFs). These constrained dynamics ease the solving of the matching conditions, which determine what energetic properties of the human body can be shaped by the available

## Summary

The majority of assistive exoskeletons are designed to rigidly track time-based kinematic patterns using highly geared actuators, which prevents users from moving their joints freely without help from the exoskeleton. Individuals with partial or full volitional control of their lower extremities require novel design and control methods for exoskeletons that are more compatible with human interaction. To assist or augment volitional human motion, exoskeleton joints must be backdrivable, and the control strategy must be invariant to the user's joint kinematics. This article presents the design philosophy behind two generations of highly backdrivable exoskeletons, which utilize torque-dense motors with low-ratio transmissions. To leverage these designs, a torque-based control framework is presented that shapes the human body's kinetic and potential energies to provide trajectory-free assistance. Simulations with a human-like biped demonstrate the effects of different energy-shaping control strategies, and experiments with a powered knee-ankle exoskeleton show the user-cooperative and task-invariant nature of the control approach. These results exhibit potential value for gait assistance and augmentation without being constrained to a clinical environment like traditional treadmill training devices. To achieve the control design and implementation, knowledge of linear algebra, robot dynamics, state-space control, and LabVIEW programming is needed.

actuators. This theoretical framework can accommodate arbitrary degrees of underactuation and system dimensions, and the resulting control law can assist any task by augmenting body energetics rather than tracking reference trajectories.

The rest of the article is organized as follows. In the next section, the design philosophy for highly backdrivable actuation systems and the mechatronic and electrical design for two generations of exoskeletons are introduced. The generalized matching framework for energy shaping with environmental and human interaction is then derived. Simulation results for different shaping strategies on an 8DOF human-like biped are presented. Finally, able-bodied human subject experiments demonstrate the backdrivability of the powered knee-ankle exoskeleton and validate the PE-shaping control strategy across a variety of locomotor tasks.

## DESIGN OF HIGHLY BACKDRIVABLE EXOSKELETONS

In this section, we present the mechatronic designs for two generations of powered exoskeletons shown in Figure 1. The required high-torque output of these devices is achieved by increasing the torque density of the electrical motor rather than the transmission ratio. The reflected inertia (or mechanical impedance) of these actuators is drastically reduced through the use of a low-ratio transmission. This actuation design is capable of controlling the output torque without any torque sensing because direct-drive and quasi-direct-drive actuation systems can be modeled as linear systems [38]. These designs are also intrinsically backdrivable

(without any sensing or control), which is ideal for human interaction. Moreover, low-impedance actuators have the potential for energy regeneration during periods of negative work [18], which helps to extend battery life or requires smaller batteries.

### Generation Zero: Powered Ankle Exoskeleton

As the first step in design, we built a powered ankle exoskeleton to validate the proposed design philosophy [33]. The hardware design presented in this section was mainly conducted to achieve high-torque output, accurate torque control performance, and low backdrive torque.

To obtain a sufficient torque output and a small torque ripple, we chose a high-torque actuator with a permanent magnetic synchronous motor (PMSM) connected to a two-stage planetary gear transmission (TPM 004X, Wittenstein, Inc., 2.4 kg, efficiency 94%). A Poly Chain GT Carbon timing belt (8MGT 720, Gates Industry, Inc., efficiency between 92.8 and 97.8%) is used to further increase actuator output torque and move the heavy weight toward the user's COM, which minimizes the metabolic burden of added weight during locomotion [39]. Given the combined transmission ratio (43.71:1), approximate efficiency (90%), and peak motor torque (1.29 Nm), the actuator's peak torque and power were estimated to be 50 Nm and 288 W, respectively. The computer-aided design rendering of the ankle exoskeleton is shown in Figure 2.

For the purpose of control implementation, we measured several features of the human's walking gait (walking phase,

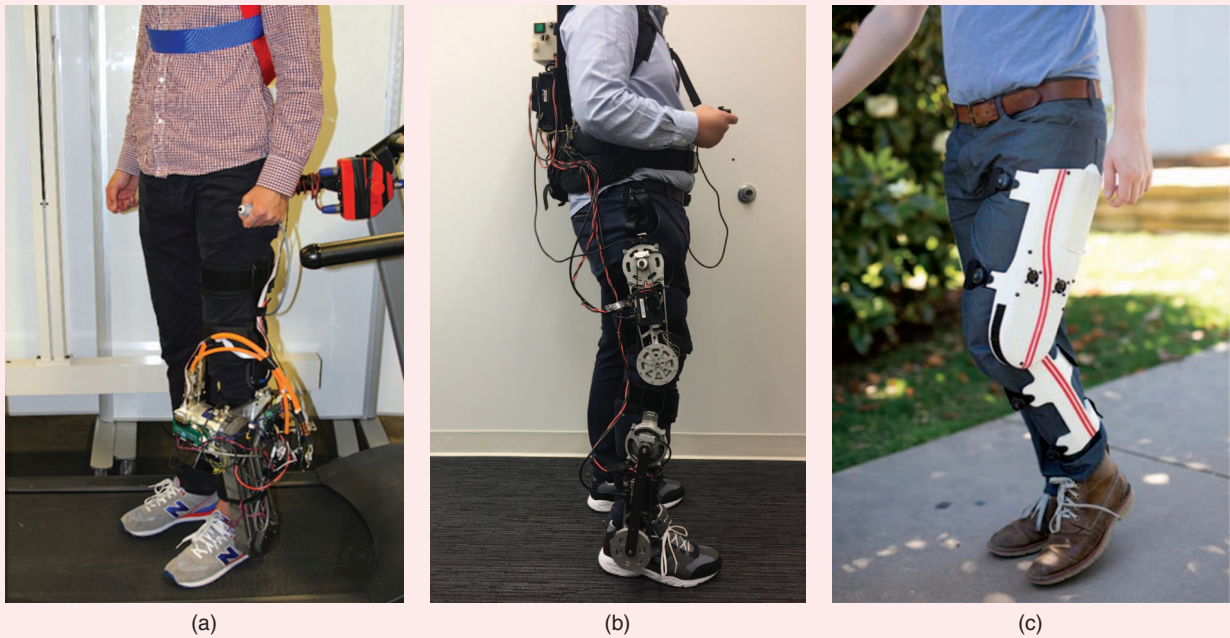


**FIGURE 1** Three generations of exoskeleton prototypes: (a) the powered ankle exoskeleton (Generation Zero; image reproduced from [33]), (b) the powered knee-ankle exoskeleton (Generation One), and (c) the powered knee exoskeleton (Generation Two). All prototypes are designed with a combination of high-torque motors and low-ratio transmissions.

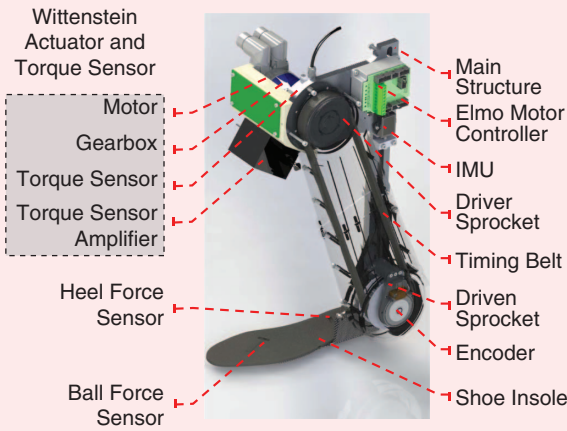


**FIGURE 2** The powered ankle exoskeleton (Generation Zero). This is a single-joint exoskeleton that provides an increased output torque to the ankle joint with small torque ripple. This is achieved by combining a permanent magnetic synchronous motor and a two-stage planetary gear transmission with a Poly Chain GT Carbon timing belt. IMU: inertial measurement unit. (Figure reproduced from [33].)

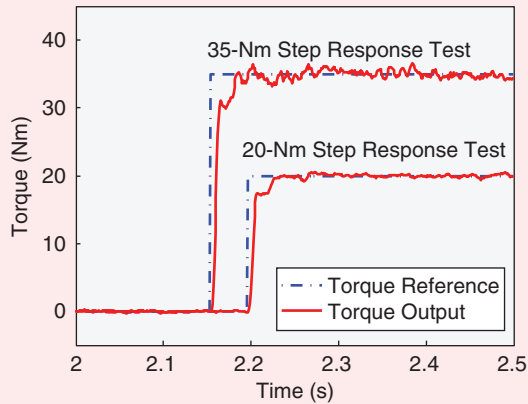


**FIGURE 3** The step response results of the ankle exoskeleton's actuator. The dashed line indicates the step reference, and the solid red line indicates the actual torque output. This test was conducted with a 35- and 20-Nm step reference, respectively. (Figure reproduced from [33].)

ankle angle, and shank angle) using the following sensors. Two force sensors (FlexiForce A301, Tekscan, Inc.) were placed in a custom shoe insole (one under the heel and the other under the ball of the foot) to detect the heel strike, midstance, and preswing phases of the gait. The insole, made from a rubber-like PolyJet photopolymer, was produced with a Connex 350 three-dimensional printer. The ankle angle was measured with an optical incremental encoder (2048 CPR, US Digital, Inc.) and the global orientation of the shank with an inertial measurement unit (IMU) (3DM-GX4-25, LORD MicroStrain, Inc.) on the main structure.

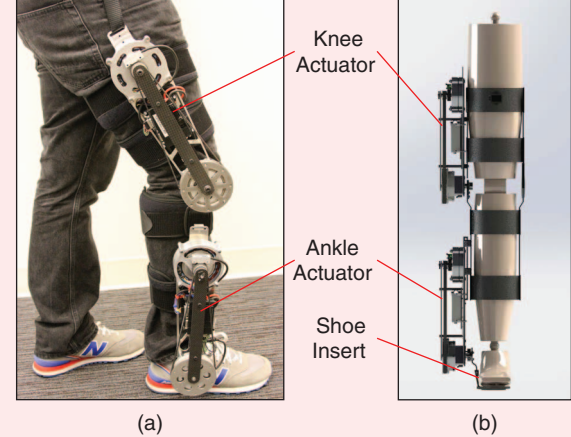


**FIGURE 4** The (a) powered knee-ankle exoskeleton and (b) its rendering. Two modular actuators are attached to a knee brace and provide torque to the knee and ankle joints of the affected leg. Torque is transferred to the ankle with the use of a small shoe insert that also houses two small pressure sensors along the center of pressure to aid the control system. (Figure reproduced from [34].)

Having designed and built the device, we conducted a torque step response test to verify the performance of the actuation system. A reaction torque sensor (TPM 004+, Wittenstein, Inc.) was installed between the actuator case and main structure to measure the real torque output from the actuator. In this experiment, the actuator was locked in place while medium-torque (20 Nm) and high-torque tests (35 Nm) were completed. The results in Figure 3 have a short response time and small steady error. The backdrivability of the device was then demonstrated by treadmill experiments with able-bodied subjects, who walked at various speeds with and without closed-loop torque control [33]. However, the use of industrial components resulted in an overall exoskeleton mass of approximately 4.5 kg, which was too heavy for a single-joint exoskeleton for mobile gait assistance. The tethered power supply and overall size also constrained the device to a stationary treadmill training environment. In the next iteration of our design philosophy, we used custom components to create a next-generation, powered, knee-ankle exoskeleton that is light enough for mobile gait assistance.

### Generation One: Powered Knee-Ankle Exoskeleton

This section introduces our second exoskeleton prototype: the powered knee-ankle exoskeleton [34] shown in Figure 4. The two actuator modules are attached to a knee-ankle-foot orthotic brace to drive the knee and ankle joints. Torque is transferred to the human ankle through a carbon fiber shoe insert. Several sensors are installed on the brace and the actuator modules to monitor key variables of the gait cycle, as shown in the block diagram of Figure 5.

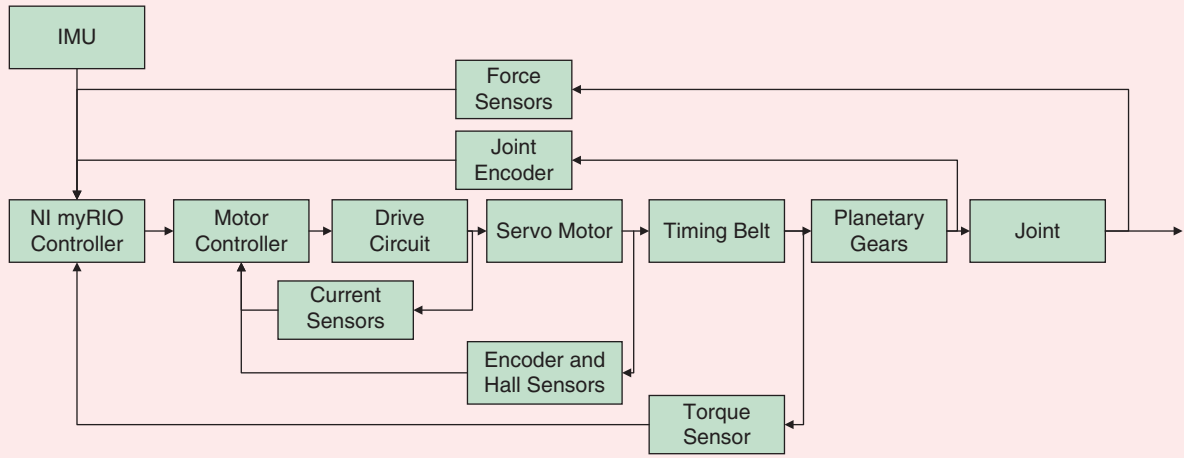


**FIGURE 5** A schematic of the powered knee-ankle exoskeleton system. A servo motor generates a torque, which is then amplified by a timing belt and a planetary gear transmission. Sensor data are fed into a myRIO controller for information processing and commanding the motor controller. IMU: inertial measurement unit. (Figure reproduced from [34].)

### Motors and Transmissions

To reduce the weight and package factor, frameless high torque-density PMSMs (that is, ac servo motors) and a custom transmission were used to provide sufficient input torque and power to the user. By optimizing the motor-winding configuration, the custom motor (MF0096008, Allied Motion, Inc.) can produce 7.2-Nm peak torque and 200 W power. A distributed two-stage, low-ratio transmission was designed for the actuator. A Poly Chain GT carbon timing belt (3MR, Gates Industry, Inc., 4:1 ratio, efficiency between 92.8 and 97.8%) was used to amplify the motor torque and to move the actuator weight closer to the user's COM. A custom 6:1 planetary gear transmission (minimum efficiency of 90% [40]) was built inside the driven sprocket of the timing belt to minimize weight and size. The overall ratio of the two-stage transmission was 24:1, with an estimated efficiency between 83.5 and 88%. The schematic of the actuator is shown in Figure 6. In theory, the combination of the torque dense motor and the distributed low-ratio transmission could produce over 150 Nm of output torque. However, the motor's torque was limited by a thermal condition, and the motor's velocity output was limited by working voltage. To balance the torque and velocity requirements, the actuation system was designed to provide 30-Nm continuous torque output with peak velocity at 80 r/min. The peak torque was limited to 60 Nm by the mechanical structure and the maximum current (30 A) of the motor driver (G-TWI-25/100-SE, Elmo Motion Control, Ltd.).

### Design of Mechanical and Electrical Systems

The frameless motor and custom transmission were integrated into the mechanical structure to further reduce the weight of the exoskeleton. For instance, the motor housing is part of the main structure of the exoskeleton, which was mainly manufactured with aluminum alloy. Several carbon fiber pieces were

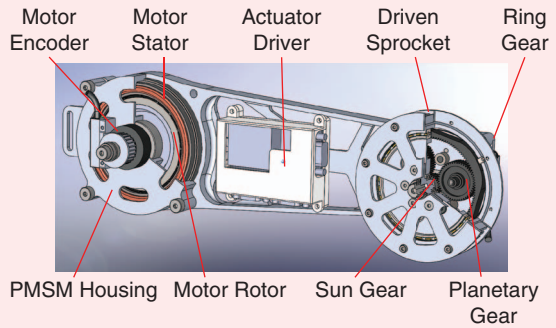


**FIGURE 6** A schematic of the modular actuator of the powered knee-ankle exoskeleton. A frameless electrical motor is integrated with the mechanical structure of the exoskeleton. A timing belt connects the output shaft of the motor to the sun gear. A planetary gear set is built inside the driven sprocket yielding a lightweight, power dense actuator. PMSM: permanent magnetic synchronous motor. (Figure reproduced from [34].)

used to reduce heavy metal materials and strengthen the actuation system. The final mass of each module (knee versus ankle) was approximately 2 kg, with detailed specifications given in Table 1. Considering only actuator components, the torque density of each actuator is approximately 50 Nm/kg. The total mass of this exoskeleton is similar to our first prototype (Generation Zero), but it includes two actuators instead of only one at the ankle. The package factor and mass characteristics were greatly improved by using frameless components.

The electrical system of this exoskeleton has two main parts: a high-level gait-control system and a low-level actuator drive system. The gait-control system monitors the key variables of the user's gait to implement any given torque-based rehabilitation control algorithm. The actuator drive

system tracks torque commands from the gait-control system, as shown in the block diagram of Figure 7.

### Torque Control System

A common method for controlling torque is based on estimating the actuator's output torque through the motor phase currents, the transmission ratio  $\xi$ , and efficiency  $\eta$ . The

**TABLE 1** The mass specifications of the powered knee-ankle exoskeleton. Note that the knee and ankle modules include the mass of onboard electronics and cabling.

Components	Mass (kg)
Knee module (thigh)	2.106
Ankle module (shank)	1.843
Shoe insert	0.356
Thigh attachment	0.632
Shank attachment	0.471
Total mass	5.41

actuator output torque  $T_a$  and electromagnetic motor torque  $T_e$  are

$$T_a = T_e \xi \eta = (3P/2) \lambda_m I_q \xi \eta, \quad (1)$$

where  $P$  is the number of motor poles,  $\lambda_m$  is the motor flux linkage, and  $I_q$  is the active current in the d-q rotating reference frame calculated by the Clarke and Park transformations [41]. Equation (1) determines the reference motor current to achieve the desired output torque, and the motor driver regulates the motor current using a proportional-integral (PI) controller in the inner loop of Figure 8. This low-level current loop operates at a much higher sampling rate than the gait-control system (approximately 10 versus 1 kHz, respectively), so its dynamics are separately controlled.

The accuracy of the torque output via (1) depends on a known transmission efficiency  $\eta$ , which can vary during dynamic motion due to different factors such as asymmetric friction loss [42]. A potential benefit of a low-ratio transmission is that the efficiency is higher and more constant

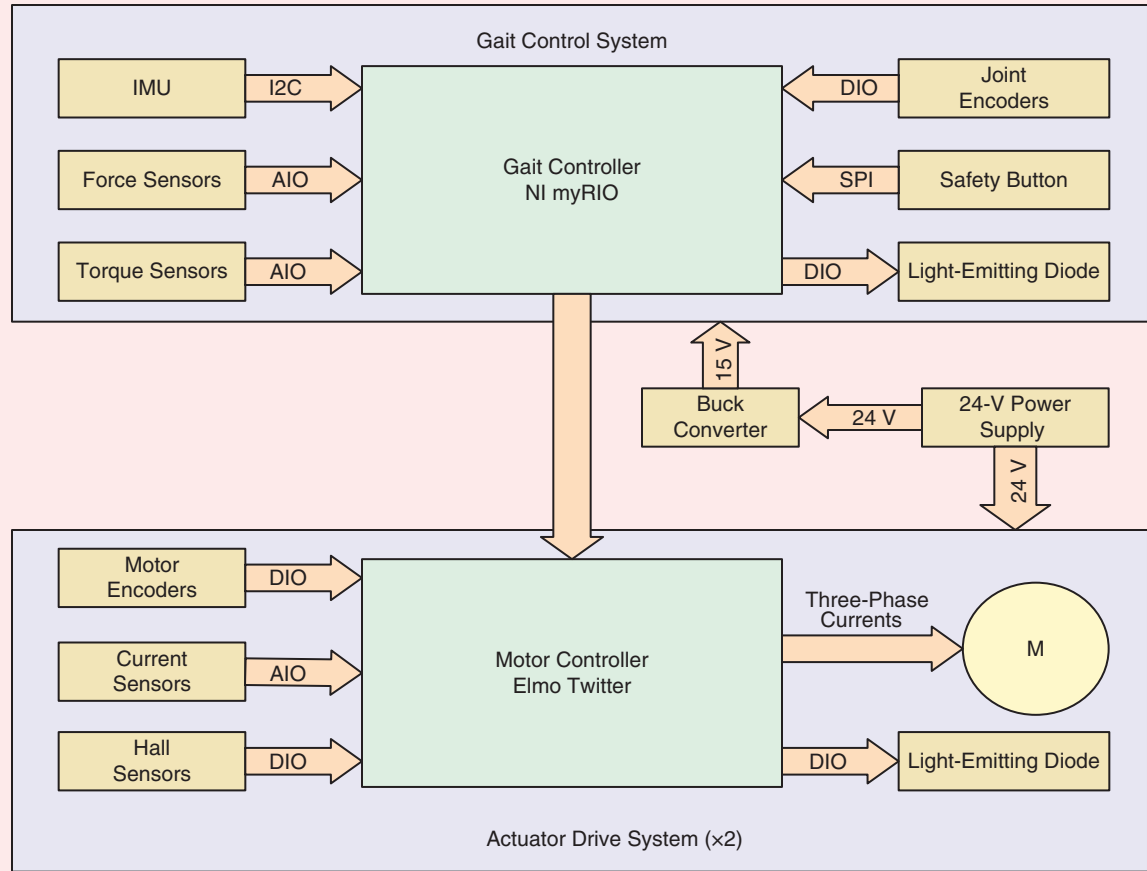


**FIGURE 7** A block diagram of the electrical system of the powered knee-ankle exoskeleton: the gait-control system receives feedback related to the user's gait and sends torque commands. The two actuator drive systems control and drive the knee and ankle actuators. A buck dc–dc converter provides power to the gait-control system. (Figure reproduced from [34].) DIO: digital input–output; AIO: analog input–output; SPI: serial peripheral interface; I2C: interintegrated circuit.

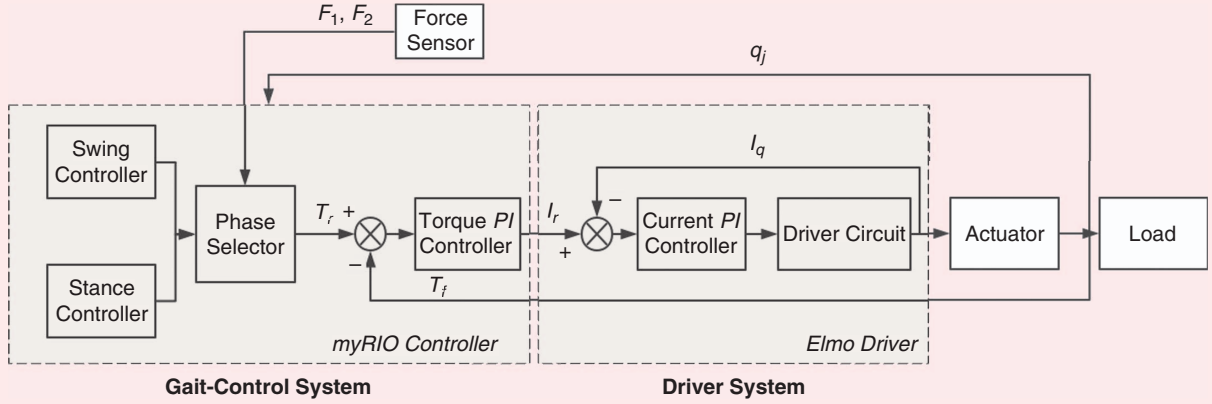


**FIGURE 8** A torque control system schematic, where  $q_j$  represents joint angles,  $F_1$  and  $F_2$  are ground reaction forces,  $T_r$  is the reference torque,  $T_f$  is the measured output torque,  $I_r$  is the reference current, and  $I_q$  is the motor's active current [41]. The phase selector switches between the stance and swing controllers, which produce the torque references. The actuator drive system contains two proportional-integral (PI) control loops. The inner loop is the current PI controller, which regulates the motor's current. The outer loop is the torque PI controller to compensate for the actuator's torque tracking error. (Figure reproduced from [34].)

(for example, fewer gears meshing [40], [43]) and, thus, improves the accuracy of current-based torque control [18]. To demonstrate this by comparison, we implemented a second (outer) torque control loop to compensate the torque error measured by a reaction torque sensor (M2210E, Sunrise Instruments Co., Ltd.) inline between the actuator and joint. Both loops (inner current loop and outer torque loop) use PI control to enforce the torque commanded by the higher-level joint control strategy. The overall control schematic is shown in Figure 8.

### Benchtop Tests

Before testing the exoskeleton on human subjects, benchtop tests were conducted to characterize the actuator's performance. We first measured the static backdrive torque, which is defined as the minimum torque required to overcome static friction to backdrive the actuator. A torque was manually applied to the output shaft of the actuator and gradually increased until rotation began. At this point, the actuator's inline reaction torque sensor measured 1.5 Nm. The backdrive torque during dynamic conditions will be reported through treadmill walking tests in the human subject experiments section.

A high-torque test was also conducted to verify the actuator's torque output and the related response time. The actuator was mounted to a testing platform, and its output shaft was mechanically fixed. Then, a low torque of 3 Nm was set to preload the actuator and ensure that any mechanical backlash would not interfere with the test. Finally, a torque of 50 Nm was commanded, maintained for 5 s, and then set back to zero. The results of this test are plotted in Figure 9. Once the system settled [ $t \geq 0.4$  in Figure 9(a)], the steady-state error was lower than 1.3%. These test results were imported into the Matlab Control and Simulation

Toolbox and used to generate a model of the system. This model suggests that the system's torque bandwidth is 10 Hz, which exceeds the required bandwidth for human walking (4–8 Hz [44]).

This design philosophy successfully balances the core requirements of volitional gait assistance: backdrivability,

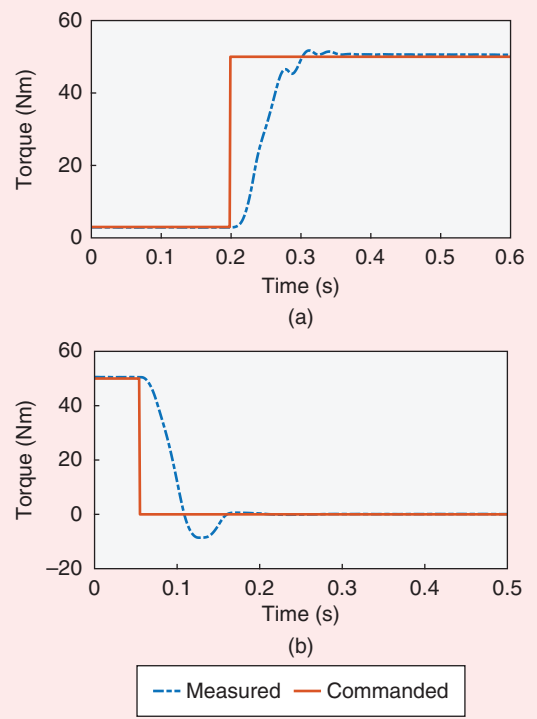


**FIGURE 9** The results from the static torque test. The figure shows the (a) rising and (b) falling edges of a 50-Nm torque step response. Note that the rising edge started from a pretension of 3 Nm.

torque-based control, high torque density, and light weight. High output torque is achieved by increasing the torque density of the electrical motor rather than increasing the transmission ratio. This low-ratio actuator design provides intrinsic backdrivability without the high cost and complexity of variable transmissions, clutches, and/or series elastic components. Our second-generation powered knee exoskeleton [Figure 1(c)] takes this design philosophy further with a lower transmission ratio (7:1 via one-stage planetary gears), which is discussed in the future work section.

## ENERGY-SHAPING CONTROL OF LOWER-LIMB EXOSKELETONS

Conventional trajectory-based control tends to provide the user with the least amount of volitional control over the device, which limits its applicability to different patient populations [45]. Instead of tracking kinematic trajectories, this section introduces a task-invariant, energetic control approach for providing exoskeletal assistance known as energy shaping. Energy shaping has been applied to biped models to facilitate natural, efficient gaits [46]–[49] based on passive dynamics. Although promising results have been shown, these works have been limited to simple toy models where the matching conditions (to be introduced later) are tractable. Similarly, these biped models have point feet or flat feet with a single contact model, often assuming full actuation. Humans are not point-footed or flat-footed walkers. In human walking, contact varies from heel to toe (resulting in multiple periods of underactuation), which cannot be captured by the existing framework. It is also unknown how to incorporate human interaction. Therefore, a complete theoretical framework for underactuated energy shaping is proposed that incorporates both environmental and human interaction.

### Energy Shaping: A Brief Review

Energy shaping is a control method that alters the dynamical characteristics of a mechanical system [50]–[54]. We briefly review the traditional concept of energy shaping. Consider a forced  $n$ -dimensional Euler–Lagrange system with configuration space  $\mathbb{Q}$  (assume  $\mathbb{R}^n$  for simplicity) and its tangent bundle  $T\mathbb{Q} = \cup_{q \in \mathbb{Q}} T_q \mathbb{Q}$ . The system can be described by a Lagrangian  $\mathcal{L}(q, \dot{q})$  defined as

$$\mathcal{L}(q, \dot{q}) = \mathcal{K}(q, \dot{q}) - \mathcal{P}(q) = \frac{1}{2} \dot{q}^T M(q) \dot{q} - \mathcal{P}(q), \quad (2)$$

where the Lagrangian  $\mathcal{L}(q, \dot{q}) : T\mathbb{Q} \rightarrow \mathbb{R}$  is a smooth function,  $q \in \mathbb{Q}$  is the generalized coordinates vector, and  $\dot{q} \in T_q \mathbb{Q}$  is the velocity vector. The scalar function  $\mathcal{K}(q, \dot{q}) : T\mathbb{Q} \rightarrow \mathbb{R}$  is the KE defined by the positive-definite mass/inertia matrix  $M(q) \in \mathbb{R}^{n \times n}$ , and  $\mathcal{P}(q) : \mathbb{Q} \rightarrow \mathbb{R}$  is the PE. The Lagrangian dynamics are given by

$$\frac{d}{dt} \partial_{\dot{q}} \mathcal{L}(q, \dot{q}) - \partial_q \mathcal{L}(q, \dot{q}) = \tau, \quad (3)$$

which can be further expressed as

$$M(q) \ddot{q} + C(q, \dot{q}) \dot{q} + N(q) = \tau, \quad (4)$$

where  $C(q, \dot{q}) \in \mathbb{R}^{n \times n}$  is the Coriolis/centrifugal matrix,  $N(q) = \nabla_q \mathcal{P}(q) \in \mathbb{R}^n$  is the gravitational forces vector, and  $\tau \in \mathbb{R}^n$  contains all external (nonconservative) forces. For the underactuated case,  $\tau = B(q)u$  where matrix  $B(q) \in \mathbb{R}^{n \times p}$  maps the control input  $u \in \mathbb{R}^p$  to the  $n$ -dimensional dynamics ( $n > p$ ).

Now consider an unforced Euler–Lagrange system defined by another Lagrangian  $\tilde{\mathcal{L}}(q, \dot{q}) : T\mathbb{Q} \rightarrow \mathbb{R}$  described as

$$\tilde{\mathcal{L}}(q, \dot{q}) = \tilde{\mathcal{K}}(q, \dot{q}) - \tilde{\mathcal{P}}(q) = \frac{1}{2} \dot{q}^T \tilde{M}(q) \dot{q} - \tilde{\mathcal{P}}(q) \quad (5)$$

with a new KE  $\tilde{\mathcal{K}}(q, \dot{q}) : T\mathbb{Q} \rightarrow \mathbb{R}$  and PE  $\tilde{\mathcal{P}}(q) : \mathbb{Q} \rightarrow \mathbb{R}$ . The resulting Lagrangian dynamics can be expressed as

$$\frac{d}{dt} \partial_{\dot{q}} \tilde{\mathcal{L}}(q, \dot{q}) - \partial_q \tilde{\mathcal{L}}(q, \dot{q}) = 0, \quad (6)$$

which can also be expressed as

$$\tilde{M}(q) \ddot{q} + \tilde{C}(q, \dot{q}) \dot{q} + \tilde{N}(q) = 0, \quad (7)$$

where  $\tilde{C}(q, \dot{q})$  is the Coriolis/centrifugal matrix in closed loop and  $\tilde{N}(q) = \nabla_q \tilde{\mathcal{P}}(q)$ .

The systems (4) and (7) match if (7) is a possible closed-loop system of (4), that is, there exists a control law  $u$  such that (4) becomes (7). Equivalently, standard results in [52] show that these two systems match if and only if there exists a full-rank left annihilator  $B(q)^\perp \in \mathbb{R}^{(n-p) \times n}$  of  $B(q)$ , that is,  $B(q)^\perp B(q) = 0$  and rank  $(B(q)^\perp) = n - p$ , for all  $q \in \mathbb{Q}$ , such that

$$B^\perp(q)[C(q, \dot{q}) \dot{q} + N(q) - M(q)\tilde{M}(q)^{-1}(\tilde{C}(q, \dot{q}) \dot{q} + \tilde{N}(q))] = 0. \quad (8)$$

The so-called matching condition is shown in (8), which is a nonlinear partial differential equation that determines the achievable closed-loop energy. Assuming (8) is satisfied, one can obtain that

$$B(q)u = M(q)\ddot{q} + C(q, \dot{q})\dot{q} + N(q) - (\tilde{M}(q)\ddot{q} + \tilde{C}(q, \dot{q})\dot{q} + \tilde{N}(q)). \quad (9)$$

Solving (7) for  $\ddot{q}$  yields the expression

$$\ddot{q} = -\tilde{M}(q)^{-1}(\tilde{C}(q, \dot{q})\dot{q} + \tilde{N}(q)). \quad (10)$$

Substituting (10) into (9) and multiplying the left-pseudo-inverse of  $B(q)$  (equivalent to matrix inverse for  $n = p$ ) on both sides of (9) yields the control law as [32]

$$u = (B(q)^T B(q))^{-1} B(q)^T \times [C(q, \dot{q})\dot{q} + N(q) - M(q)\tilde{M}(q)^{-1}(\tilde{C}(q, \dot{q})\dot{q} + \tilde{N}(q))]. \quad (11)$$

### Interacting with the Environment

The matching condition (8) is trivially satisfied for all  $\tilde{M}(q)$  and  $\tilde{\mathcal{P}}(q)$  if  $n = p$ , that is, if the system is fully actuated [32].

When the system is underactuated ( $n > p$ ), solutions of the matching condition become difficult to obtain [55]. Contact constraints affect the number of unactuated coordinates and, therefore, must be considered when deriving energy-shaping control laws. In this section, generalized dynamics with contact constraints are presented, and the corresponding matching conditions are derived. First, a planar biped that combines the human body and exoskeleton(s) is modeled. For simplicity, the torso and hip are combined as a single mass (that is, only one hip joint). However, the following framework can also be used with more human-like models.

### Modeling the Biped

The biped is modeled as a kinematic chain with respect to an inertial reference frame (IRF) shown in Figure 10. Depending on whether the exoskeleton is unilateral or bilateral, the stance and swing legs are modeled separately (unilateral case [35], [36]) or the entire lower body as a kinematic chain from the stance foot to the swing foot (bilateral case [37]). By explicitly modeling contact constraints in the dynamics, the equations of motion can be expressed as

$$M(q)\ddot{q} + C(q, \dot{q})\dot{q} + N(q) + A(q)^T\lambda = \tau, \quad (12)$$

where  $M(q) \in \mathbb{R}^{n \times n}$ ,  $C(q, \dot{q}) \in \mathbb{R}^{n \times n}$ , and  $N(q) \in \mathbb{R}^{n \times 1}$  are defined similar to the terms in (4). The configuration vector is  $q = (\theta_x, \theta_y, \theta_{ab}, q_s^T)^T \in \mathbb{R}^n$ , where  $\theta_x$  and  $\theta_y$  are the Cartesian coordinates with respect to the IRF,  $\theta_{ab}$  is an absolute angle defined with respect to the vertical axis, and the shape vector  $q_s \in \mathbb{R}^{n-3}$  contains joint angles based on the biped model (to be specified in the simulation section.) The matrix  $A(q)^T \in \mathbb{R}^{n \times c}$  is the constraint matrix defined as the gradient of the holonomic constraint functions (see "Holonomic Contact Constraints"), and  $c$  is the number of contact constraints depending on the contact condition. The Lagrange multiplier  $\lambda$  is calculated using the method in [15], [56] as

$$\begin{aligned} \lambda &= \hat{\lambda} + \bar{\lambda}\tau, \text{ where} \\ \hat{\lambda} &= W(q)(\dot{A}(q)\dot{q} - A(q)M(q)^{-1}C(q,\dot{q})\dot{q} - A(q)M(q)^{-1}N(q)), \\ \bar{\lambda} &= W(q)A(q)M(q)^{-1}, \text{ with } W(q) = (A(q)M(q)^{-1}A(q)^T)^{-1}. \end{aligned} \quad (13)$$

Because the human body and exoskeleton are combined, the torque  $\tau = \tau_{hum} + \tau_{exo}$  on the right-hand side of (12) comprises the human input terms  $\tau_{hum} = B(q)v + J(q)^T F$  and the exoskeleton input  $\tau_{exo} = B(q)u$ . The mapping matrix  $B(q) \in \mathbb{R}^{n \times p}$  maps both the human muscular torques  $v \in \mathbb{R}^p$  and the exoskeleton actuator torques  $u \in \mathbb{R}^p$  into the dynamics. Without loss of generality, assume  $B(q)$  takes the form of  $[0_{p \times (n-p)}, I_{p \times p}]^T$ . The force vector  $F = (F_x, F_y, M_z)^T \in \mathbb{R}^{3 \times 1}$  in  $\tau_{hum}$  denotes the interaction forces between the stance model and the swing leg model, where  $(F_x, F_y)^T$  and  $M_z$  indicate the two linear forces and a moment in the sagittal plane, respectively. The forces  $F$  are mapped into the dynamics by the

body Jacobian matrix  $J(q)^T \in \mathbb{R}^{n \times 3}$ . Note that for bilateral exoskeleton models, the interaction forces  $F$  are internal to the dynamics of the complete kinematic chain and, hence, will not appear as an external input (that is,  $F = 0$ ).

### Holonomic Contact Constraints

In the previous section, we explicitly modeled contact in the dynamics without specifying the choice of contact constraints. In this section, the general form of holonomic contact constraints encountered during the single-support period of human walking are defined, which are expressed as relations between the position variables  $a(q_1, q_2, \dots, q_c) = 0_{c \times 1}$ , where  $q_i$  denotes the  $i$ th element of the configuration vector  $q$ . The single-support period can be separated into heel-contact, flat-foot, and toe-contact phases, based on which appropriate holonomic contact constraints can be defined, as in

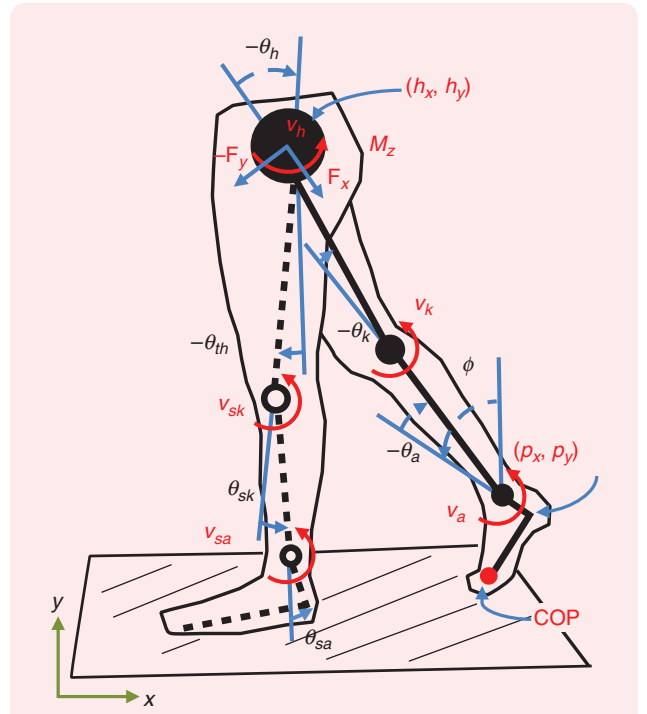


**FIGURE 10** A kinematic model of the human body and the exoskeleton(s). The stance leg is shown in solid black, and the swing leg (just before impact) in dashed black. For controlling a unilateral exoskeleton, the stance and swing legs are separately modeled. The stance leg is modeled as a kinematic chain from the inertial reference frame, which is defined at the stance heel during heel and flat-foot contact versus the stance toe during toe contact. As for the swing leg, the hip is chosen as a floating base for the swing leg's kinematic chain.  $F = (F_x, F_y, M_z)^T \in \mathbb{R}^{3 \times 1}$  are the interaction forces between the hip of the stance model and the swing thigh. For modeling a human wearing a bilateral exoskeleton, the stance and swing-leg models (full biped model) are combined, and the forces  $F$  are implicitly modeled in the equations of motion of the complete kinematic chain. For simulations of the full biped model, the angle  $\theta_h$  is defined as the hip angle between the stance and swing thighs, and the red arcs indicate the human muscle inputs. COP: center of pressure.

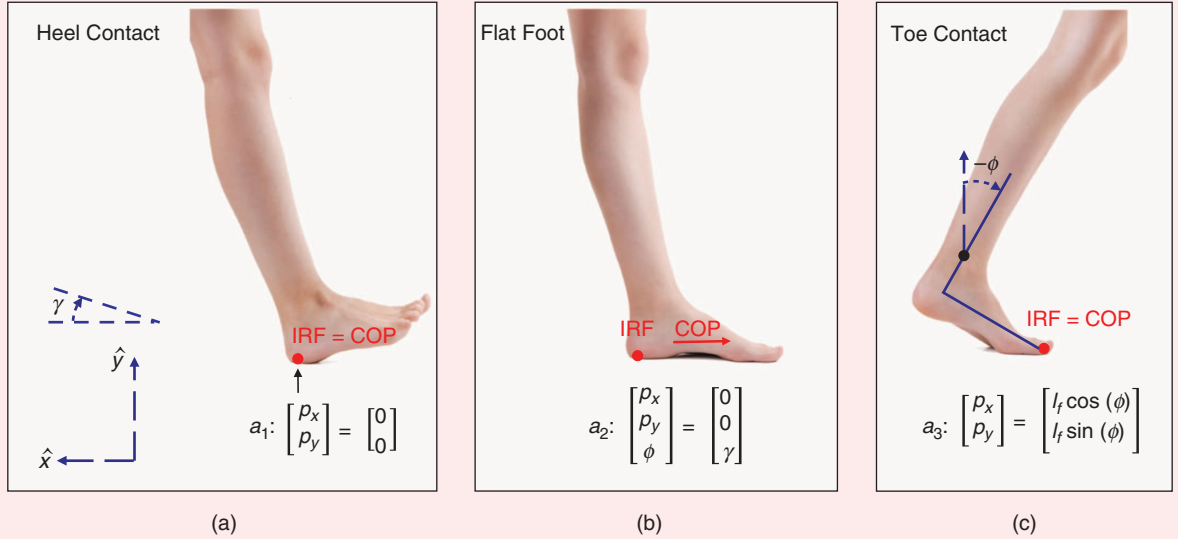


**FIGURE 11** The (a) heel-contact, (b) flat-foot, and (c) toe-contact configurations during the single-support period of human locomotion. For simulation purposes, the biped is assumed to be walking on a slope with angle  $\gamma$ . To have a constant constraint matrix  $A$ , the inertial reference frame can be moved to the toe during toe contact, that is,  $(t_x, t_y)^T = [p_x - l_f \cos(\phi), p_y - l_f \sin(\phi)]^T = (0, 0)^T$ , where  $(t_x, t_y)^T$  denotes the position of the toe. COP: center of pressure.

Figure 11. There are  $c = 2$  constraints for heel and toe contacts, whereas flat foot has  $c = 3$ . It is shown later that the proposed framework is able to accommodate arbitrary numbers of contact constraints. In this article, the constraint matrix  $A(q)$  has the constant form

$$A(q) = \nabla_q a(q_1, q_2, \dots, q_c) = [I_{c \times c} \ 0_{c \times (n-c)}]. \quad (14)$$

This constant form (that is,  $\dot{A} = 0$ ) can be achieved by defining the IRF at the stance toe during toe contact and the stance heel during heel and flat foot contact.

#### Equivalent Constrained Dynamic

The classical matching condition (8) and control law (11) in the previous section cannot be directly applied to the generalized dynamics (12). Although a dynamical system in the form of (4) could be separately modeled for each phase by dropping constrained coordinates from the generalized coordinate vector, this would require a change of coordinates for some constraints (for example, rolling contact [57]). The dimension and degree of underactuation of the resulting hybrid system also changes between phases, requiring different models for control law (11). Switching between control models in real time requires precise estimates of the gait cycle phase, which can be difficult to achieve in practice [14].

Instead of modeling a different dynamical system for each phase, the results of the previous sections are extended to a single generalized system (12) to obtain a shaping framework that can accommodate any holonomic contact constraints (and the resulting unactuated DOFs) that could occur during various locomotor tasks. This generalized

framework shows what terms can and cannot be shaped with each contact constraint. The proposed approach begins by substituting expressions for  $A(q)$  and  $\lambda$  into (12) to obtain the form of (4), which is known as the ECD that have fewer (possibly zero) unactuated DOFs compared to the generalized dynamics (12) without constraints. Moving forward,  $q$  and  $\dot{q}$  are omitted in the dynamical terms to abbreviate notations. Following the procedure in [37], the equivalent constrained form of (12) is expressed as

$$M_\lambda \ddot{q} + C_\lambda \dot{q} + N_\lambda = B_\lambda v + J_\lambda^T F + B_\lambda u, \quad (15)$$

$$\begin{aligned} \text{where } M_\lambda &= M, \\ C_\lambda &= (I - A^T WAM^{-1})C + \tilde{A}^T W \dot{A}, \\ N_\lambda &= (I - A^T WAM^{-1})N, \\ B_\lambda &= (I - A^T WAM^{-1})B, \\ J_\lambda^T &= (I - A^T WAM^{-1})J^T. \end{aligned} \quad (16)$$

Given the open-loop dynamics (15), the desired closed-loop ECD is defined as

$$\tilde{M}_\lambda \ddot{q} + \tilde{C}_\lambda \dot{q} + \tilde{N}_\lambda = \tilde{\tau}_{\text{hum}}, \quad (17)$$

where  $\tilde{M}_\lambda = \tilde{M}$  is the mass/inertia matrix in the closed-loop ECD and is assumed to be positive-definite. The remaining terms in (17) are given by

$$\begin{aligned} \tilde{C}_\lambda &= (I - A^T \tilde{W} \tilde{A} \tilde{M}^{-1}) \tilde{C} + \tilde{A}^T \tilde{W} \dot{\tilde{A}}, \\ \tilde{N}_\lambda &= (I - A^T \tilde{W} \tilde{A} \tilde{M}^{-1}) \tilde{N}, \\ \tilde{B}_\lambda &= (I - A^T \tilde{W} \tilde{A} \tilde{M}^{-1}) \tilde{B}, \\ \tilde{J}_\lambda^T &= (I - A^T \tilde{W} \tilde{A} \tilde{M}^{-1}) \tilde{J}^T, \\ \tilde{W} &= (A \tilde{M}^{-1} A^T)^{-1}, \end{aligned} \quad (18)$$

where  $\tilde{C}$  and  $\tilde{N}$  are the dynamics terms of (12) in closed loop. We denote the closed-loop human input vector as  $\tilde{B}_{\lambda}v + \tilde{J}_{\lambda}^T F$ , but we make no assumptions on the human inputs  $v$  and  $F$ . Instead, these two terms are assumed to be mapped into the closed-loop dynamics by  $\tilde{B}_{\lambda}$  and  $\tilde{J}_{\lambda}^T$  to be defined next.

### Matching Based on Equivalent Constrained Dynamics

This section introduces the generalized matching condition based on ECD. Given (15) and (17), the procedure from (4) to (8) are followed to derive the matching condition for the ECD as

$$B_{\lambda}^\perp [M_{\lambda}\tilde{M}_{\lambda}^{-1}(\tilde{B}_{\lambda}v + \tilde{J}_{\lambda}^T F - \tilde{C}_{\lambda}\dot{q} - \tilde{N}_{\lambda}) + C_{\lambda}\dot{q} + N_{\lambda} - B_{\lambda}v - J_{\lambda}^T F] = 0, \quad (19)$$

which can be separated into submatching conditions that correspond to matching for KE, PE, and human inputs, respectively:

$$B_{\lambda}^\perp(C_{\lambda}\dot{q} - M_{\lambda}\tilde{M}_{\lambda}^{-1}\tilde{C}_{\lambda}\dot{q}) = 0, \quad (20)$$

$$B_{\lambda}^\perp(N_{\lambda} - M_{\lambda}\tilde{M}_{\lambda}^{-1}\tilde{N}_{\lambda}) = 0, \quad (21)$$

$$B_{\lambda}^\perp[B_{\lambda}v + J_{\lambda}^T F - M_{\lambda}\tilde{M}_{\lambda}^{-1}(\tilde{B}_{\lambda}v + \tilde{J}_{\lambda}^T F)] = 0. \quad (22)$$

#### Matching for Kinetic Energy

Prior research showed that the bottom-right submatrix of a mass matrix is the mass matrix of a lower-dimensional mechanical system [58]. This motivates shaping of the bottom-right part in  $M_{\lambda}$ , which may render matching conditions that are easier to satisfy. Following the procedure in [35], [36],  $M_{\lambda}$  is decomposed into matrices blocks

$$M = \begin{bmatrix} M_1 & M_2 \\ M_2^T & M_4 \end{bmatrix} = M_{\lambda}, \quad (23)$$

where  $M_1 \in \mathbb{R}^{c \times c}$ ,  $M_2 \in \mathbb{R}^{c \times (n-c)}$ . The bottom-right part should be shaped via control; hence, we define the closed-loop inertia matrix as

$$\tilde{M} = \begin{bmatrix} M_1 & M_2 \\ M_2^T & \tilde{M}_4 \end{bmatrix} = \tilde{M}_{\lambda}, \quad (24)$$

where the choice of  $\tilde{M}_4$  will be specified in the following sections.

References [32] and [55] provide the relationship between  $C$  and  $M$  as

$$C\dot{q} = D_q(M\dot{q})\dot{q} - \frac{1}{2}\partial_q(\dot{q}^T M \dot{q}), \quad (25)$$

where  $D_x(y)$  is the Jacobian matrix of partial derivatives of vector  $y$  with respect to vector  $x$ . Because the first  $c$  DOFs are constrained, their time derivatives equal zero, so that (25) reduces to

$$C\dot{q} = D_q \begin{bmatrix} M_2 \dot{q}_{c+1,n} \\ M_4 \dot{q}_{c+1,n} \end{bmatrix} \begin{bmatrix} 0 \\ \dot{q}_{c+1,n} \end{bmatrix} - \frac{1}{2}\partial_q(\dot{q}_{c+1,n}^T M_4 \dot{q}_{c+1,n}),$$

where the subscript  $(i, j)$  indicates rows  $i$  through  $j$  of a matrix. Note that the submatrix  $M_4$  does not depend on  $q_{1,c}$ , based on the recursively cyclic property in [58], yielding simplified expressions for  $C\dot{q}$  and  $\tilde{C}\dot{q}$  as

$$C\dot{q} = \begin{bmatrix} \partial_{q_{c+1,n}}(M_2 \dot{q}_{c+1,n}) \dot{q}_{c+1,n} \\ \Psi \end{bmatrix}, \quad (26)$$

$$\tilde{C}\dot{q} = \begin{bmatrix} \partial_{q_{c+1,n}}(M_2 \dot{q}_{c+1,n}) \dot{q}_{c+1,n} \\ \Psi \end{bmatrix}, \quad (27)$$

where

$$\Psi := \frac{1}{2}\partial_{q_{c+1,n}}(\dot{q}_{c+1,n}^T M_4 \dot{q}_{c+1,n}) \in \mathbb{R}^{(n-c) \times 1},$$

$$\tilde{\Psi} := \frac{1}{2}\partial_{q_{c+1,n}}(\dot{q}_{c+1,n}^T \tilde{M}_4 \dot{q}_{c+1,n}) \in \mathbb{R}^{(n-c) \times 1}.$$

Following the same procedure in [36],  $[I - A^T WAM^{-1}]$  is calculated in (15) using the blockwise inversion of  $M$ , and  $[I - A^T \tilde{WAM}^{-1}]$  is defined accordingly as

$$[I - A^T WAM^{-1}] = \begin{bmatrix} 0_{c \times c} & Y \\ 0_{(n-c) \times c} & I_{(n-c) \times (n-c)} \end{bmatrix}, \quad (28)$$

$$[I - A^T \tilde{WAM}^{-1}] = \begin{bmatrix} 0_{c \times c} & \tilde{Y} \\ 0_{(n-c) \times c} & I_{(n-c) \times (n-c)} \end{bmatrix}, \quad (29)$$

where  $Y = M_2 M_4^{-1}$  and  $\tilde{Y} = M_2 \tilde{M}_4^{-1}$ . Multiplying (28) with (26) and (29) with (27) yields

$$C_{\lambda}\dot{q} = \begin{bmatrix} Y\Psi \\ \Psi \end{bmatrix}, \quad \tilde{C}_{\lambda}\dot{q} = \begin{bmatrix} \tilde{Y}\tilde{\Psi} \\ \tilde{\Psi} \end{bmatrix}. \quad (30)$$

To simplify the multiplication between  $M_{\lambda}$  and  $\tilde{M}_{\lambda}^{-1}$ , the blockwise inversion method is applied again to obtain

$$M_{\lambda}\tilde{M}_{\lambda}^{-1} = \begin{bmatrix} I_{c \times c} & 0_{c \times (n-c)} \\ \Omega_1 & \Omega_2 \end{bmatrix}, \quad (31)$$

where  $\Omega_1 = (I - M_4 \tilde{M}_4^{-1})M_2^T (M_1 - M_2 \tilde{M}_4^{-1} M_2^T)^{-1} \in \mathbb{R}^{(n-c) \times c}$  and  $\Omega_2 = -\Omega_1 \tilde{Y} + M_4 \tilde{M}_4^{-1} \in \mathbb{R}^{(n-c) \times (n-c)}$ . The matrix  $B_{\lambda}$  is calculated from (16), and its annihilator  $B_{\lambda}^\perp$  can be chosen as

$$B_{\lambda} = \begin{bmatrix} YB_{c+1,n} \\ B_{c+1,n} \end{bmatrix}, \quad B_{\lambda}^\perp = \begin{bmatrix} I_{c \times c} & -Y \\ 0_{(n-p-c) \times c} & S \end{bmatrix}, \quad (32)$$

where  $S = [I_{(n-p-c) \times (n-p-c)}, 0_{(n-p-c) \times p}]$ . When the system is fully constrained (that is,  $n = p + c$ ), the second block row of the annihilator disappears. It can be verified that  $B_{\lambda}^\perp \in \mathbb{R}^{(n-p) \times n}$ ,  $\text{rank}(B_{\lambda}^\perp) = n - p$ , and  $B_{\lambda}^\perp B_{\lambda} = 0_{(n-p) \times p}$ . Substituting  $B_{\lambda}^\perp$ , (31), and (30) into (20), the left-hand side of the matching condition becomes

$$B_{\lambda}^\perp [C_{\lambda}\dot{q} - M_{\lambda}\tilde{M}_{\lambda}^{-1}\tilde{C}_{\lambda}\dot{q}] = \begin{bmatrix} I_{c \times c} & -Y \\ 0_{(n-p-c) \times c} & S \end{bmatrix} \begin{bmatrix} Y\Psi - \tilde{Y}\tilde{\Psi} \\ \Psi - \Omega_1 \tilde{Y}\tilde{\Psi} - \Omega_2 \tilde{\Psi} \end{bmatrix}. \quad (33)$$

The first  $c$  rows of (33) can be simplified as

$$\begin{aligned}
& [I_{c \times c} - Y] \begin{bmatrix} Y\Psi - \tilde{Y}\Psi \\ \Psi - \Omega_1 \tilde{Y}\Psi - \Omega_2 \tilde{\Psi} \end{bmatrix} \\
& = (-\tilde{Y} + Y\Omega_1 \tilde{Y} + Y\Omega_2) \tilde{\Psi} \\
& = (-\tilde{Y} + YM_4 \tilde{M}_4^{-1}) \tilde{\Psi} \\
& = (-\tilde{Y} + M_2 \tilde{M}_4^{-1}) \tilde{\Psi} = 0_{c \times 1}.
\end{aligned} \quad (34)$$

For contacts (for example, heel or toe contact) that result in underactuation ( $n > p + c$ ), additional analysis is needed to fully satisfy the matching condition (20), that is, the bottom ( $n - p - c$ ) rows of (33) must also be satisfied.

Note that during underactuated cases,  $M_4$  cannot be shaped arbitrarily. We propose satisfying the matching condition by shaping only the bottom-right  $p \times p$  part of  $M_4$ , which is associated with the  $p$  actuated coordinates. To demonstrate this,  $M_4$  is first decomposed and then shaped in a manner similar to (24) as

$$M_4 = \begin{bmatrix} M_{41} & M_{42} \\ M_{42}^T & M_{44} \end{bmatrix}, \quad \tilde{M}_4 = \begin{bmatrix} M_{41} & M_{42} \\ M_{42}^T & \tilde{M}_{44} \end{bmatrix},$$

where  $M_{41} \in \mathbb{R}^{(n-p-c) \times (n-p-c)}$ ,  $M_{42} \in \mathbb{R}^{(n-p-c) \times p}$ , and  $M_{44}, \tilde{M}_{44} \in \mathbb{R}^{p \times p}$ . Similar to (31), the top-left element of  $M_4 \tilde{M}_4^{-1}$  will be  $I_{(n-p-c) \times (n-p-c)}$ . Subtracting  $M_4 \tilde{M}_4^{-1}$  from  $I_{(n-c) \times (n-c)}$ , the first ( $n - p - c$ ) rows of  $\Omega_1$  will become zeroes. As a consequence, the first ( $n - p - c$ ) rows of  $\Omega_2$  become  $[I_{(n-p-c) \times (n-p-c)}, 0_{(n-p-c) \times p}]$ . Leveraging these properties of  $\Omega_1$  and  $\Omega_2$ , the bottom ( $n - p - c$ ) rows of (33) become

$$\begin{aligned}
& [0_{(n-p-c) \times c} \ S] \begin{bmatrix} Y\Psi - \tilde{Y}\Psi \\ \Psi - \Omega_1 \tilde{Y}\Psi - \Omega_2 \tilde{\Psi} \end{bmatrix} \\
& = \frac{1}{2} \partial_{q_{c+1,n-p}} (\dot{q}_{c+1,n}^T (M_4 - \tilde{M}_4) \dot{q}_{c+1,n}). \quad (35)
\end{aligned}$$

From [58], it is shown that  $\partial M_{44} / \partial q_{c+1,n-p} = 0$ , that is,  $q_{c+1,n-p}$  is cyclic in  $M_{44} \in \mathbb{R}^{p \times p}$ . Hence, (35) equals  $0_{(n-p-c) \times 1}$ , and the matching condition (20) is satisfied.

### Matching for Potential Energy

The constrained potential forces vectors are obtained from (16) and (18) as

$$N_\lambda = \begin{bmatrix} YN_{c+1,n} \\ N_{c+1,n} \end{bmatrix}, \quad \tilde{N}_\lambda = \begin{bmatrix} \tilde{Y}\tilde{N}_{c+1,n} \\ \tilde{N}_{c+1,n} \end{bmatrix}. \quad (36)$$

The choices of desired gravitational forces vector  $\tilde{N}_{c+1,n}$  will be specified later. Similar to the matching proof for KE, substituting  $B_\lambda^\perp$ , (31), and (36) into (21), the first  $c$  rows of the matching condition are derived as

$$\begin{aligned}
& [I_{c \times c} - Y] [N_\lambda - M_\lambda \tilde{M}_\lambda^{-1} \tilde{N}_\lambda] \\
& = [I_{c \times c} - Y] \begin{bmatrix} YN_{c+1,n} - \tilde{Y}\tilde{N}_{c+1,n} \\ N_{c+1,n} - \Omega_1 \tilde{Y}\tilde{N}_{c+1,n} - \Omega_2 \tilde{N}_{c+1,n} \end{bmatrix} \\
& = (-\tilde{Y} + Y\Omega_1 \tilde{Y} + Y\Omega_2) \tilde{N}_{c+1,n} = 0_{c \times 1},
\end{aligned} \quad (37)$$

which can be verified based on (34). Again, (37) serves as the matching condition (21) for the fully actuated conditions. For underactuated cases, the additional ( $n - p - c$ )

rows of the matching condition are verified, which can be expressed as

$$\begin{aligned}
& [0_{(n-p-c) \times c} \ S] [N_\lambda - M_\lambda \tilde{M}_\lambda^{-1} \tilde{N}_\lambda] \\
& = S \cdot (N_{c+1,n} - \Omega_1 \tilde{Y}\tilde{N}_{c+1,n} - \Omega_2 \tilde{N}_{c+1,n}) \\
& = N_{c+1,n-p} - \tilde{N}_{c+1,n-p},
\end{aligned} \quad (38)$$

where the properties of  $\Omega_1$  and  $\Omega_2$  in (31) are leveraged. As in [35], this matching condition can be satisfied by assuming  $N_{c+1,n-p} = \tilde{N}_{c+1,n-p}$ , which are the rows that correspond to the unactuated DOFs that are unconstrained. The same assumption is made here to satisfy the matching condition (21).

### Matching for Human Inputs

Because the human joint input  $v$  and the interaction forces  $F$  are not easily measured in practice, we choose the closed-loop mappings  $\tilde{B}$  and  $\tilde{J}^T$ , such that  $v$  and  $F$  disappear from the exoskeleton control law and the matching condition (22) is satisfied. Specifically, the equations  $B_\lambda^\perp (B_\lambda - M_\lambda \tilde{M}_\lambda^{-1} \tilde{B}_\lambda) = 0$  and  $B_\lambda^\perp (J_\lambda^T - M_\lambda \tilde{M}_\lambda^{-1} \tilde{J}_\lambda^T) = 0$  are solved for

$$\tilde{B}_{c+1,n} = \tilde{M}_4 M_4^{-1} B_{c+1,n}, \quad (39)$$

$$\tilde{J}_{c+1,n}^T = \tilde{M}_4 M_4^{-1} J_{c+1,n}^T. \quad (40)$$

These terms immediately satisfy the matching condition (22) and alter the way that the human joint inputs  $v$  and interaction forces  $F$  enter the closed-loop system dynamics. Given (39) and (40), the control law that brings (15) into (17) becomes

$$u = (B_\lambda^\perp B_\lambda)^{-1} B_\lambda^\perp [C_\lambda \dot{q} + N_\lambda - M_\lambda \tilde{M}_\lambda^{-1} (\tilde{C}_\lambda \dot{q} + \tilde{N}_\lambda)]. \quad (41)$$

### Energy-Shaping Strategies: Compensating Inertia and Body Weight

The main mechanical tasks that require energy during human walking are 1) supporting the body's weight during stance, 2) driving the body's COM against inertia, 3) swinging the legs, and 4) maintaining balance. A percentage of the subject's weight is typically offloaded using an overhead BWS harness during gait rehabilitation to reduce the muscular force required for the first task. While the harness can offload the human weight that needs to be supported by the stance leg, there is no straightforward way to offload the human swing leg's weight. Not being able to compensate for swing leg mass can have consequences such as the foot drop phenomenon in poststroke individuals. A second limitation of the conventional BWS strategy is that COM and leg inertia compensation are not possible. Braking forces at heel strike decelerate the COM, which again needs to be accelerated during the drive phase. A study of the independent effects of weight and mass on the metabolic cost of walking [59] found that driving the

**Before testing the exoskeleton on human subjects, benchtop tests were conducted to characterize the actuator's performance.**

COM against inertia accounts for up to 50% of the total metabolic cost. KE-shaping assistance from an exoskeleton could potentially reduce this metabolic cost, and prior work [31] indicates that inertia compensation can counteract the side effects of the exoskeleton inertia on human legs during walking.

These facts motivate the compensation for the limb inertia and body weight in the shapeable parts of ECD. To this end,  $\tilde{M}_4$  and  $\tilde{N}$  are chosen by scaling the limb moments of inertia in  $M_4 \in \mathbb{R}^{p \times p}$  and the gravity constant in the shapeable part of  $N$

$$\tilde{M}_4 = M_D + \kappa \cdot M_I, \quad (42)$$

$$\tilde{N} = [N_{1,n-p}^T, \tilde{N}_{n-p+1,n}^T]^T = [N_{1,n-p}^T, \mu N_{n-p+1,n}^T]^T, \quad (43)$$

where  $M_D \in \mathbb{R}^{p \times p}$  and  $M_I \in \mathbb{R}^{p \times p}$  are matrices that correspond to the translational and rotational portions of  $M_4$ , respectively [60]. Note that matrix  $M_I$  is constant and only contains limb moments of inertia. The nonnegative scaling factor  $\kappa$  is chosen lower than one to compensate limb inertia ( $\tilde{M}_4 < M_4$ , so that  $\tilde{M}_4 - M_4$  is negative definite) or greater than one to add virtual limb inertia ( $\tilde{M}_4 > M_4$ , so that  $\tilde{M}_4 - M_4$  is positive definite) in closed loop. However, it is important to ensure that  $\tilde{M}_4$  remains positive definite during inertia compensation to avoid singularities in the control law. Finally, the positive scaling factor  $\mu$  is chosen to be lower than one for positive BWS ( $\tilde{g} < g$ ) or greater than one for negative BWS ( $\tilde{g} > g$ ), where  $g = 9.81 \text{ m/s}^2$  is the gravity constant in the gravitational forces vector  $N$ .

### Passivity and Stability

Energy shaping is intimately related to the notion of passivity [50]–[53], through which safe interactions between the exoskeleton and the human user can be guaranteed (see “Passivity and Stability Properties” for more details). Input–output passivity implies that the change in some storage quantity (often energy) is bounded by the energy injected through the input. That is, the system cannot generate energy on its own. It was shown in [36] that the human-exoskeleton system is passive from the human inputs to joint velocity after shaping PE (Figure 12). This implies that energy growth is controlled by the human, and thus interaction with the exoskeleton should be safe. In particular, it is possible to establish Lyapunov stability results for commonly assumed human control policies [36]. This passivity result also holds for the case of total energy shaping, which is left to future work.

### SIMULATIONS OF ENERGY-SHAPING CONTROL ON A HUMAN-LIKE BIPED

Now that controllers have been designed for the study of the exoskeleton, the study of simulated walking with the full biped model in Figure 10 is required. This requires consideration of the coupled dynamics of the two legs [15]. The full biped is modeled as a kinematic chain with respect to the IRF defined at the stance heel with the configuration vector  $q = (\theta_x, \theta_y, \theta_{ab}, q_s^T)^T = (p_x, p_y, \phi, \theta_a, \theta_k, \theta_h, \theta_{sk}, \theta_{sa})^T \in \mathbb{R}^8$ .  $(\theta_x, \theta_y)^T = (p_x, p_y)^T$  is chosen as the Cartesian coordinates of the stance heel and  $\theta_{ab} = \phi$  as the stance heel angle defined with respect to the vertical axis. In the shape vector  $q_s = (\theta_a, \theta_k, \theta_h, \theta_{sk}, \theta_{sa})^T$ ,  $\theta_a$  and  $\theta_{sa}$  are the angles of the stance and swing ankle,  $\theta_k$  and  $\theta_{sk}$  are angles of the stance and swing knee, and  $\theta_h$  is the hip angle between the stance and swing thighs. In this section, we simulate the full biped model, assuming it is wearing a bilateral exoskeleton with three different shaping strategies: PE, KE, and total energy.

### Impedance Control for Human Inputs

To predict the effects of the proposed control approach, we first construct a human-like, stable walking gait in simulation. According to the results in [61], a simulated seven-link biped can converge to a stable, natural-looking gait using joint impedance control. The control torque of each joint can be constructed from a spring damper coupled with phase-dependent equilibrium points [62]. This control paradigm is adopted to generate dynamic walking gaits that preserve the ballistic swing motion [63] and the energetic efficiency down slopes [64], which are characteristic of human locomotion. It is assumed that the human has input torques at the ankle, knee, and hip joints. For simplicity, the human impedance parameters remain constant instead of having a different set of parameters with respect to each phase of stance, as in [62]. The human input vector  $\tau_{\text{hum}}$  for the full biped model is

$$\tau_{\text{hum}} = [0_{1 \times 3}, v_a, v_k, v_h, v_{sk}, v_{sa}]^T \in \mathbb{R}^{8 \times 1}, \quad (44)$$

where  $v_j$  is the human torque for joint  $j \in \{a, k, h, sk, sa\}$  and is

$$v_j = -K_{pj}(q_j - \bar{q}_j) - K_{dj}\dot{q}_j, \quad (45)$$

where  $K_{pj}$ ,  $K_{dj}$ ,  $q_j$ , and  $\bar{q}_j$  correspond to the stiffness, viscosity, actual angle, and equilibrium angle of joint  $j$ , respectively.

## Passivity and Stability Properties

Consider an  $n$ -link robot described by the following equations of motion:

$$M(q)\ddot{q} + C(q, \dot{q})\dot{q} + N(q) = \tau, \quad (\text{S1})$$

where  $q \in \mathbb{R}^n$  is the configuration vector, and  $\dot{q} \in \mathbb{R}^n$  is the velocity vector. The positive-definite matrix  $M(q) \in \mathbb{R}^{n \times n}$  is the mass/inertia matrix,  $C(q, \dot{q}) \in \mathbb{R}^{n \times n}$  is the Coriolis/centrifugal matrix,  $N(q) \in \mathbb{R}^n$  is the gravitational forces vector defined as the gradient of the robot's potential energy (PE), and  $\tau \in \mathbb{R}^n$  is the torque input vector.

Let  $S(x) : \mathbb{R}^n \rightarrow \mathbb{R}$  be a continuously differentiable nonnegative scalar function; then the system (S1) is said to be passive from input  $\tau$  to output  $y$  with storage function  $S(x)$  if  $\dot{S}(x) \leq y^T \tau$ . Passivity indicates that the change in the robot's energy is bounded by the energy injected through the input  $\tau$ . In other words, the robot cannot generate energy on its own. For robots with dynamics of the form (S1), input–output passivity can be shown by choosing  $y = \dot{q}^T$  and the robot's total energy  $H(q, \dot{q})$  as the storage function

$$H(q, \dot{q}) = \frac{1}{2}\dot{q}^T M(q)\dot{q} + P(q). \quad (\text{S2})$$

Taking the time derivative of  $H(q, \dot{q})$  yields

$$\begin{aligned} \dot{H} &= \dot{q}^T M(q)\ddot{q} + \frac{1}{2}\dot{q}^T \dot{M}(q)\dot{q} + \dot{q}^T N(q) \\ &= \dot{q}^T (\tau - C(q, \dot{q})\dot{q} - N(q)) + \frac{1}{2}\dot{q}^T \dot{M}(q)\dot{q} + \dot{q}^T N(q), \end{aligned}$$

where  $M(q)\ddot{q}$  has been substituted using the equations of motion (S1). Canceling out  $\dot{q}^T N(q)$  and collecting terms yields

$$\dot{H} = \dot{q}^T \tau + \frac{1}{2}\dot{q}^T (\dot{M}(q) - 2C(q, \dot{q}))\dot{q} = \dot{q}^T \tau, \quad (\text{S3})$$

where the second equality holds true based on the skew-symmetry property between  $M(q)$  and  $C(q, \dot{q})$ , that is,  $\dot{M}(q) - 2C(q, \dot{q}) = -(\dot{M}(q) - 2C(q, \dot{q}))^T$  [S1].

Input–output passivity enables several stability results through passivity-based control. For example, negative feedback of the output through the input guarantees asymptotic convergence of the output to zero [S1]. We first leverage a standard result for passive systems to state Proposition 1 [S2].

### Proposition 1

Consider the passive system (S1) with input  $\tau$  and output  $y = \dot{q}$ . Given output feedback control  $\tau = \sigma(y)$ , where  $\sigma$  is any continuous function satisfying  $y^T \sigma(y) \leq 0$ ; then  $\lim_{t \rightarrow \infty} y(t) \rightarrow 0$ , and the origin  $(q, \dot{q}) = (0, 0)$  is stable in the sense of Lyapunov.

Here, one possible stability result from [S3] is highlighted for the case of PE shaping. In [S3], we proved that PE shaping preserves the passive mapping from the human input  $\tau_{\text{hum}}$  to output  $y = \dot{q}^T$  in closed loop. This proof relies on the closed-loop total energy  $\tilde{H}$  as the storage function

$$\tilde{H}(q, \dot{q}) = \frac{1}{2}\dot{q}^T M(q)\dot{q} + \tilde{P}(q), \quad (\text{S4})$$

where  $\tilde{P}(q) := \int_0^q \sum_{i=1}^n \tilde{N}_{(i)}(s) ds$  is the closed-loop PE.

It is well established that human motor control effectively modulates joint impedance, that is, the stiffness and viscosity of a joint [S4], [S5]. Therefore, in [S3] the human input is assumed to take the form of an impedance controller (which is used for the simulations in this article) given by  $\tau_{\text{hum}} = -K_p e - K_d \dot{e}$ , where  $K_p$  and  $K_d$  are two positive-definite diagonal matrices,  $e := q - \bar{q}$  is the difference between  $q$  and the fixed equilibria vector  $\bar{q}$ , and  $\dot{e} = \dot{q} = y$ . To utilize Lyapunov stability analysis, a Lyapunov function is defined as

$$V(q, \dot{q}) = \tilde{H}(q, \dot{q}) + \frac{1}{2}e^T K_p e - c, \quad (\text{S5})$$

where  $c$  is a non-negative constant such that  $V$  is equal to zero at the equilibrium point where  $\tilde{N}(q) = -K_p e$ , that is, where the shaped gravitational forces balance the muscular spring forces. It is clear that adding a quadratic term  $(1/2)e^T K_p e$  to the positive-definite  $\tilde{H}(q, \dot{q})$  produces a positive-definite function about this equilibrium point. Taking the time derivative of  $V(q, \dot{q})$  yields

$$\begin{aligned} \dot{V}(q, \dot{q}) &= y^T \tau_{\text{hum}} + \dot{e}^T K_p e \\ &= y^T (-K_p e - K_d \dot{e} + K_p e) \\ &= -y^T K_d y \leq 0, \end{aligned} \quad (\text{S6})$$

implying that the shaped human leg is Lyapunov stable [S6].

## REFERENCES

- [S1] M. Spong, S. Hutchinson, and M. Vidyasagar, *Robot Modeling and Control*, vol. 3. Hoboken, NJ: Wiley, 2006.
- [S2] R. Sepulchre, M. Jankovic, and P. V. Kokotovic, *Constructive Non-linear Control*. New York: Springer, 2012.
- [S3] G. Lv and R. D. Gregg, "Underactuated potential energy shaping with contact constraints: Application to a powered knee-ankle orthosis," *IEEE Trans. Control. Syst. Technol.*, vol. 26, no. 1, pp. 181–193, Jan. 2018.
- [S4] T. Flash and N. Hogan, "The coordination of arm movements: An experimentally confirmed mathematical model," *J. Neurosci.*, vol. 5, no. 7, pp. 1688–1703, July 1985.
- [S5] E. Burdet, R. Osu, D. W. Franklin, T. E. Milner, and M. Kawato, "The central nervous system stabilizes unstable dynamics by learning optimal impedance," *Nature*, vol. 414, no. 6862, pp. 446–449, 2001.
- [S6] R. M. Murray, Z. Li, and S. S. Sastry, *A Mathematical Introduction to Robotic Manipulation*. Boca Raton, FL: CRC Press, 1994.

## Hybrid Dynamics and Stability

Biped locomotion can be modeled as a hybrid dynamical system that includes continuous and discrete dynamics. Impacts happen when the swing heel contacts the ground and, subsequently, when the flat foot impacts the ground. The corresponding impact equations map the state of the biped at the instant before impact to the state at the instant after impact. Note that no impact occurs when switching between the flat-foot and toe-contact configurations, but the location of the IRF does change from heel to toe to maintain a constant constraint matrix  $A$ . On the basis of the method in [15], the hybrid dynamics and impact maps during one step are computed in the following sequence:

- 1)  $M\ddot{q} + C\dot{q} + N + A_{\text{heel}}^T \lambda = \tau_{\text{exo}} + \tau_{\text{hum}}$  if  $a_{\text{flat}} \neq 0$
- 2)  $\dot{q}^+ = (I - M^{-1}A_{\text{flat}}^T(A_{\text{flat}}M^{-1}A_{\text{flat}}^T)^{-1}A_{\text{flat}})\dot{q}^-$  if  $a_{\text{flat}} = 0$
- 3)  $M\ddot{q} + C\dot{q} + N + A_{\text{flat}}^T \lambda = \tau_{\text{exo}} + \tau_{\text{hum}}$  if  $|c_p(q, \dot{q})| < l_f$
- 4)  $\dot{q}^+ = \dot{q}^-, (q(1)^+, q(2)^+)^T = \mathcal{G}$  if  $|c_p(q, \dot{q})| = l_f$
- 5)  $M\ddot{q} + C\dot{q} + N + A_{\text{toe}}^T \lambda = \tau_{\text{exo}} + \tau_{\text{hum}}$  if  $h(q) \neq 0$
- 6)  $(q^+, \dot{q}^+) = \mathcal{T}(q^-, \dot{q}^-)$  if  $h(q) = 0$ ,

where  $M \in \mathbb{R}^{8 \times 8}$ ,  $C \in \mathbb{R}^{8 \times 8}$ , and  $N \in \mathbb{R}^8$  are the dynamics terms of the full biped model. The terms  $A_{\text{heel}}$ ,  $A_{\text{flat}}$ , and  $A_{\text{toe}}$  denote the constraint matrices for the heel contact, flat foot, and toe contact conditions depicted in Figure 11, and the superscripts minus and plus indicate values before and after each impact. The term  $\mathcal{G} = (l_f \cos(\gamma), l_f \sin(\gamma))^T$  models the change in IRF for foot length  $l_f$ . The vector  $c_p(q, \dot{q})$  is the center of pressure defined with respect to the heel IRF calculated using the conservation law of momentum. The ground clearance of the swing heel is denoted by  $h(q)$ , and  $\mathcal{T}$  denotes the swing-heel ground-strike impact map derived based on [65]. The aforementioned sequence of continuous and discrete dynamics repeats after a complete step, that is, phase 6 switches back to phase 1 for the next step.

The combination of nonlinear differential equations and discontinuous events makes stability difficult to prove analytically for hybrid systems in general. Fortunately, the method of Poincaré sections [66] provides analytical conditions for local stability that can be checked numerically by simulation. Letting  $x = (q^T, \dot{q}^T)^T$  be the state vector of the full biped, a walking gait corresponds to a periodic solution curve  $\tilde{x}(t)$  of the hybrid system, such that  $\tilde{x}(t) = \tilde{x}(t + T)$ , for all  $t \geq 0$  and some minimal  $T > 0$ . The set of states occupied by the periodic solution defines a periodic orbit  $O := \{x | x = \tilde{x}(t) \text{ for some } t\}$  in the state space. The step-to-step evolution of a solution curve can be modeled with the Poincaré map  $\mathcal{P}: G \rightarrow G$ , where  $G = \{x | h(q) = 0\}$  is the switching surface indicating initial heel contact [15]. The intersection of a periodic orbit with the switching surface is a fixed point  $x^* = \mathcal{P}(x^*) = O \cap G$  with standard assumptions in [66]. If  $x^*$  is a locally exponentially stable fixed point of the discrete system  $x(k+1) = \mathcal{P}(x(k))$ , then  $O$  is a locally exponentially stable periodic orbit of the hybrid

system defining the Poincaré map  $\mathcal{P}: G \rightarrow G$ . Therefore, the periodic orbit  $O$  is locally exponentially stable if the eigenvalues of the Jacobian  $\nabla_x \mathcal{P}(x^*)$  are within the unit circle.

The Jacobian eigenvalues can be numerically calculated through a perturbation analysis as described in [67], [68]. In fact, a similar analysis using normal kinematic variability instead of explicit perturbations has shown that human walking is orbitally stable [69]. The simulations of the next section will show that the energy-shaping controller maintains the orbital stability of a nominal walking gait, which suggests that human walking will remain orbitally stable with an exoskeleton utilizing this control strategy.

## Simulation Results and Discussion

To find a stable limit cycle of the biped, the model parameters of Table 2 were chosen to consist of average values from adult males reported in [70], with the trunk masses grouped at the hip as in [15]. The foot length was set to 0.2 m to provide reasonable amounts of time in both the flat-foot and toe-contact conditions. The human joint impedance gains were first tuned by trial and error to find a stable nominal gait, where the final gains are given in Table 2. Once the stable nominal gait was found, these impedance parameters were kept constant to isolate the effects of different energy shaping controllers. In Figure 13, the knee and ankle trajectories over four steady-state strides are shown in (a), and the periodic orbit of the biped during one steady step is shown in the phase portrait of (b). Energy-shaping controllers with different shaping strategies were implemented on this biped model to study their effects.

## Phase Portraits and Gait Characteristics

The simulation results are shown with three different shaping strategies. To obtain the control law for the simulation, (42) and (43) are substituted into (11). Then,  $\mu = 1$  is set, so that  $\tilde{N} = N$  and  $\kappa$  is progressively changed to study the effects of KE shaping on the biped. Then,  $\kappa = 1$  is fixed and  $\mu$  is altered to identify the independent effects of PE shaping. Finally, both terms were concurrently increased or decreased to observe the effects of total energy shaping. For

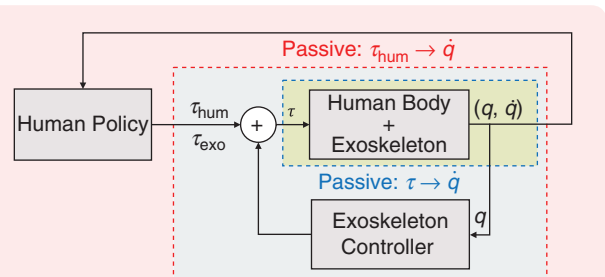


**FIGURE 12** Feedback loops and passive mappings of a human leg wearing an energy-shaping exoskeleton, where  $\tau_{\text{hum}}$  is the total human input,  $\tau_{\text{exo}}$  is the exoskeleton input,  $\tau = \tau_{\text{exo}} + \tau_{\text{hum}}$  is the combined human-exoskeleton input, and  $(q, \dot{q})$  contain the joint angles and velocities of the leg. (Figure reproduced from [36].)

**TABLE 2** The model and simulation parameters of the biped model in Figure 10. The physical parameters represent average values of male adults, and impedance parameters were kept constant during simulation. This table is reproduced from [36].

Parameter	Variable	Value
Hip mass	$m_h$	31.73 kg
Thigh mass	$m_t$	9.457 kg
Shank mass	$m_s$	4.053 kg
Foot mass	$m_f$	1 kg
Thigh moment of inertia	$I_t$	0.1995 kg·m <sup>2</sup>
Shank moment of inertia	$I_s$	0.0369 kg·m <sup>2</sup>
Full biped shank length	$l_s$	0.428 m
Full biped thigh length	$l_t$	0.428 m
Full biped heel length	$l_a$	0.07 m
Full biped foot length	$l_f$	0.2 m
Slope angle	$\gamma$	0.095 rad
Hip equilibrium angle	$\bar{\theta}_h$	-0.5 rad
Hip proportional gain	$K_{ph}$	182.258 Nm/rad
Hip derivative gain	$K_{dh}$	35.1 Nm·s/rad
Swing knee equilibrium angle	$\bar{\theta}_{sk}$	0.2 rad
Swing knee proportional gain	$K_{psk}$	182.258 Nm/rad
Swing knee derivative gain	$K_{dsk}$	18.908 Nm·s/rad
Swing ankle equilibrium angle	$\bar{\theta}_{sa}$	-0.25 rad
Swing ankle proportional gain	$K_{psa}$	182.258 Nm/rad
Swing ankle derivative gain	$K_{dsa}$	0.802 Nm·s/rad
Stance ankle equilibrium angle	$\bar{\theta}_a$	0.01 rad
Stance ankle proportional gain	$K_{pa}$	546.774 Nm/rad
Stance ankle derivative gain	$K_{da}$	21.257 Nm·s/rad
Stance knee equilibrium angle	$\bar{\theta}_k$	-0.05 rad
Stance knee proportional gain	$K_{pk}$	546.774 Nm/rad
Stance knee derivative gain	$K_{dk}$	21.257 Nm·s/rad

each specific combination of  $\kappa$  and  $\mu$ , the biped was allowed to converge to a steady gait before recording data. For notational purposes,  $0 \leq \kappa < 1$  indicates providing  $(1 - \kappa) \cdot 100\%$  support for compensating limb inertia, whereas  $\kappa > 1$  indicates adding  $(\kappa - 1) \cdot 100\%$  virtual limb inertia in closed loop. Analogously,  $0 < \mu < 1$  indicates the exoskeleton is providing  $(1 - \mu) \cdot 100\%$  BWS ( $\tilde{g} < g$ ), while  $\mu > 1$  indicates the exoskeleton is providing  $(\mu - 1) \cdot 100\%$  negative BWS ( $\tilde{g} > g$ ).

For a joint-level perspective, Figure 14 compares the phase portraits of the passive gait and shaped gaits with different shaping strategies. Wider orbits for all joints correspond to longer steps and taller orbits for all joints correspond to faster steps. For the case of KE shaping [Figure 14(a)],

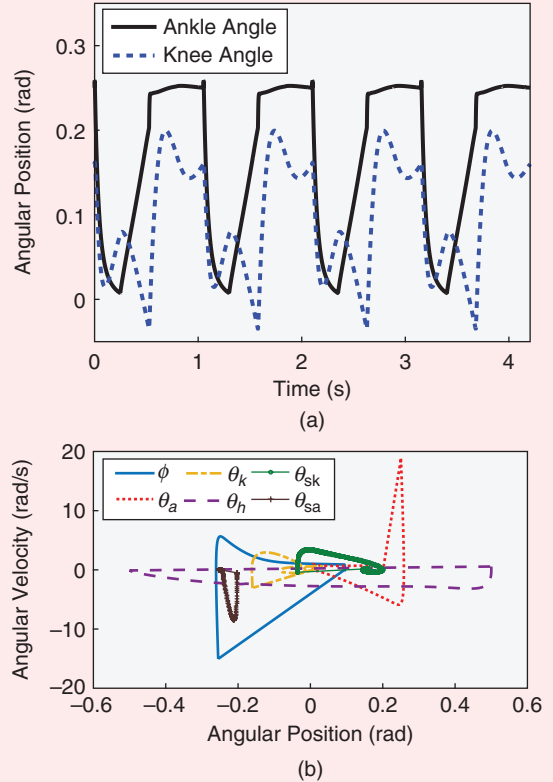


**FIGURE 13** (a) Knee and ankle trajectories of one leg over four steady-state strides of the nominal “human” gait and (b) the phase portrait of the biped during one steady step. (Figure reproduced from [36].)

maximum limb inertia compensation ( $\kappa = 0$ ) provides greater range of motion and faster joint velocities. The opposite effect is observed for most joints (except the hip) when virtually adding limb inertia ( $\kappa = 1.2$ ). The PE-shaping case [Figure 14(b)] provides the opposite trend: Positive BWS ( $0 < \mu < 1$ ) contracts the phase portraits, whereas negative BWS ( $\mu > 1$ ) expands them. This verifies the observation in [36] that decreasing PE tends to slow down the biped and constrict its range of motion, which has the benefit of greater swing foot clearance to compensate for drop foot. Decreasing (or increasing) both KE and PE through total energy shaping [Figure 14(c)] renders even greater differences than the potential shaping case (as found in [37]).

To further compare the changes in gait characteristics, the step length, step linear velocity, and step time periods recorded during simulation are shown with different shaping strategies in Table 3. Compensating body mass and/or limb inertia in the shapable dynamics with PE shaping and/or total energy shaping decreases the step length as well as the step linear velocity but increases the time periods spent for each step. In contrast, adding virtual body mass and/or limb inertia increases step length and step linear velocity but reduces time interval for each step. Although some of the joint orbits in Figure 14 expanded when compensating limb inertia with KE

shaping only ( $\kappa = 0$ ), step length and walking speed decreased because of a contraction in the hip orbit (that is, reduced hip extension causes a shorter step [71]). A similar observation holds for the case of  $\kappa = 1.2$ . These simulation results indicate that different shaping strategies can be chosen based on training goals to promote different gait characteristics.

### Metabolic Cost

A key metric for evaluating an exoskeleton is whether it reduces the human user's metabolic cost of walking [72]. The integral of electromyography (EMG) squared readings from the soleus and vastus lateralis muscles are a good representation of total metabolic cost [73]. Assuming EMG activation is directly related to joint torque production, the

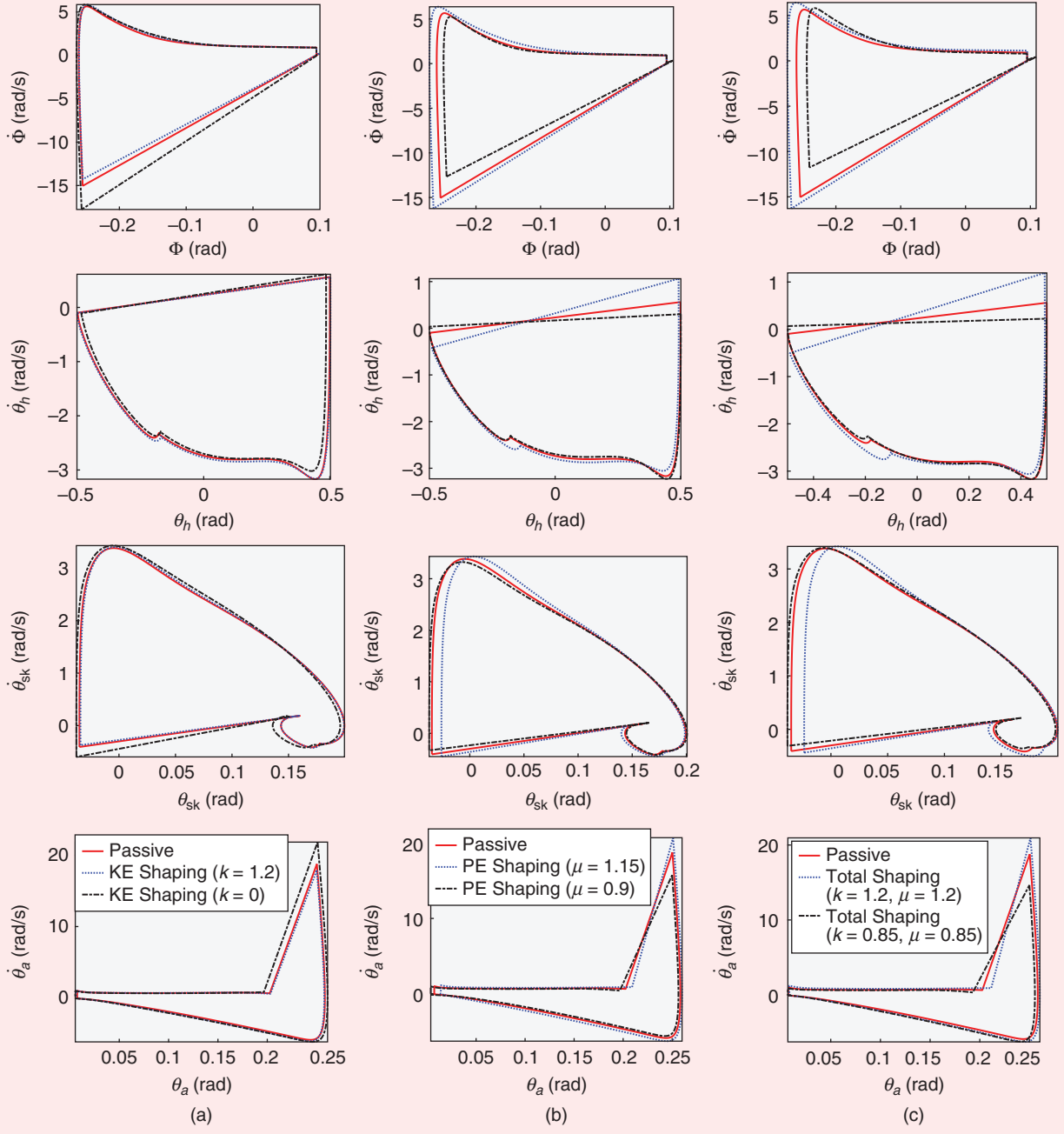


**FIGURE 14** Phase portraits of the passive gait and the shaped gaits. (a) The case of kinetic energy (KE) shaping, (b) the case of potential energy (PE) shaping, and (c) the case of total energy shaping. Each column shares the same legend as shown in the last figure. The rows (from top to bottom) correspond to  $\dot{\phi}$ , stance hip, swing knee, and stance ankle joints, respectively. Each data point on these curves was recorded once steady walking had been achieved.

**TABLE 3** Step length, step linear velocity, and step time periods recorded in simulation with different shaping strategies. KE: kinetic energy; PE: potential energy.

Control Strategies	Step Length (m)	Step Linear Velocity (m/s)	Step Time Periods (s)
Passive ( $\mu = \kappa = 1$ )	0.5259	1.0113	0.5256
PE ( $\mu = 1.1$ )	0.5379	1.1049	0.4868
PE ( $\mu = 1.05$ )	0.5352	1.0554	0.5071
PE ( $\mu = 0.95$ )	0.5281	0.9740	0.5421
PE ( $\mu = 0.9$ )	0.5264	0.9492	0.5546
KE ( $\kappa = 2$ )	0.5677	1.2598	0.4506
KE ( $\kappa = 1.2$ )	0.5368	1.0286	0.5219
KE ( $\kappa = 0.8$ )	0.5259	0.9996	0.5261
KE ( $\kappa = 0$ )	0.5114	0.9807	0.5214
Total ( $\kappa = 1.2$ , $\mu = 1.2$ )	0.5424	1.2044	0.4504
Total ( $\kappa = 0.85$ , $\mu = 0.85$ )	0.5197	0.9335	0.5567

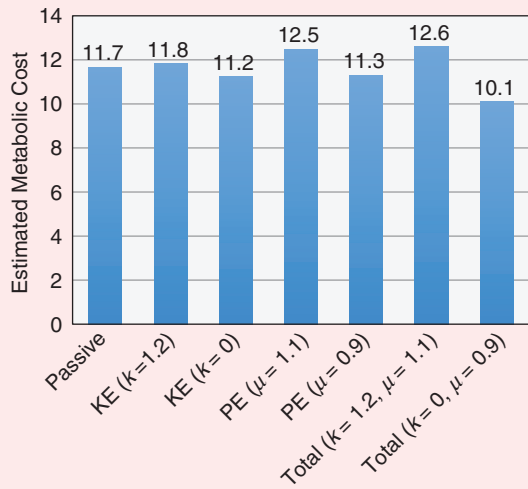


**FIGURE 15** The estimated metabolic costs with different shaping strategies. The numbers on top of each bar denote the sum of (46) for all actuated human joints given the shaping strategy indicated on the x axis. KE: kinetic energy; PE: potential energy.

authors of [74] proposed a simulation-based metric for metabolic cost

$$\alpha_j^2 = \frac{\int_0^T v_j^2(t) dt}{T(mgl)^2} \approx \frac{\sum_{i=1}^{N_T} v_j^2(i) \Delta t(i)}{T(mgl)^2}, \quad (46)$$

where  $T$  is the step time period,  $N_T$  is the number of timesteps in the simulation,  $v_j$  is the joint moment,  $m$  is the overall mass of the biped, and  $l$  is the length of the biped

**TABLE 4** Analysis of the Froude number. The first column contains different values of  $\mu$  used in the simulation. The second column contains the step linear velocities observed in simulations with the corresponding  $\mu$ , where each data point was recorded once steady walking had been achieved. The third column contains the predicted linear velocities  $\dot{s}$  calculated by multiplying the passive gait's velocity  $\dot{s} = 1.011$  m/s with  $\sqrt{\mu} = \sqrt{g/9.81}$ . PE: potential energy.

Control Strategies	Step Velocity (m/s)	Predicted Velocity $\dot{s}$ (m/s)
PE ( $\mu = 0.9$ )	0.949	0.959
PE ( $\mu = 0.95$ )	0.974	0.985
Passive ( $\mu = 1$ )	1.011	1.011
PE ( $\mu = 1.05$ )	1.055	1.036
PE ( $\mu = 1.1$ )	1.105	1.060

leg. Therefore, the sum of all human joint costs (46) are computed to estimate the effects of energy shaping on the metabolic cost of walking, where several different conditions are shown in Figure 15.

From Figure 15, it is shown that adding 20% virtual limb inertia (KE,  $\kappa = 1.2$ ) has minor effects on the metabolic cost compared to the passive gait, whereas compensating all the limb inertia (KE,  $\kappa = 0$ ) reduces the metabolic cost. Similarly, for the case of PE shaping, negative BWS (PE,  $\mu = 1.1$ ) increases the biped's metabolic cost, whereas positive BWS (PE,  $\mu = 0.9$ ) reduces the overall metabolic cost compared to the passive gait. This meets the expectation that offloading the weight of a patient makes it easier to practice walking. For total energy shaping,  $\kappa = 1.2$  and  $\mu = 1.1$  made the biped consume more metabolic energy than only shaping KE with  $\kappa = 1.2$  or PE with  $\mu = 1.1$ . When compensating limb inertia in addition to gravity by total energy shaping ( $\kappa = 0$ ,  $\mu = 0.9$ ), the biped consumed the least amount of energy compared to all the other cases in Figure 15. These results suggest that the energy-shaping approach could provide meaningful assistance during gait rehabilitation, where a clinician can adjust the scaling factors to actively manipulate human effort.

### Froude Number

The Froude number quantifies the optimal exchange between KE and PE during dynamic locomotion [75] and has been used to predict the effect of different gravity constants on walking gaits [76]. Two geometrically similar bodies that make use of the exchange between KE and PE to move (for example, pendular motion) will behave in a dynamically similar manner if they are associated with the same Froude number  $F_r = \dot{s}^2/gl$ , where  $\dot{s}$  is the velocity of progression [75],  $l$  is leg length, and  $g$  is the gravity constant. Assuming  $F_r$  remains constant, the effect of gravity on walking speed was predicted by  $\dot{s} = \dot{s}\sqrt{(\tilde{g}/g)}$  in [76]. Therefore, varying gravity  $\tilde{g}$  will affect the optimal walking

speed  $\dot{s}$ , such that increased gravity will result in higher velocity and vice versa [77]. To determine whether the simulation results agreed with this trend, predicted velocities  $\dot{s}$  were calculated with different values of  $\tilde{g}$ , where  $\dot{s}$  was the velocity at  $\mu = 1$  (passive gait). The results in Table 4 show that the trend predicted by the Froude number was maintained in the simulation.

## HUMAN SUBJECT EXPERIMENTS WITH POWERED KNEE-ANKLE EXOSKELETON

Having demonstrated simulation results on a human-like biped, the energy-shaping control approach was implemented on the powered knee-ankle exoskeleton to validate the proposed design and control philosophy. This unilateral device was designed to assist poststroke individuals who usually have impairments on one side of their body, such as diminished leg muscle strength or the inability to generate voluntary muscle contractions with normative magnitude [78]. This section first verifies that the device is sufficiently backdrivable during the dynamic conditions of locomotion. Then, a PE-shaping controller is implemented to provide BWS and demonstrate experimental results with an able-bodied subject performing three different activities of daily living. The human subject experiments followed a protocol approved by the institutional review board of The University of Texas at Dallas. During these experiments, the subject had the ability to deactivate the exoskeleton by releasing a handheld safety switch.

### Dynamic Backdrive Torque Test

During dynamic conditions, backdrive torques must be large enough to overcome the reflected inertia and reflected damping of the actuator, which scale with the gear ratio squared [18]. The low-ratio actuator design of the powered knee-ankle exoskeleton aimed to minimize the reflected inertia and damping for improved dynamic backdrivability. This was accomplished by monitoring the reaction torque sensors inline with the actuators during dynamic walking conditions with the command torque of both joints set to zero. An able-bodied human subject began this test with active torque compensation enabled, that is, using the outer torque loop in Figure 8. After several steps, the user released the safety button to deactivate the actuator and walked without active torque compensation.

The absolute backdrive torques (averaged over ten steps) with and without compensation are shown in Figure 16. The peak dynamic backdrive torque is lower than 8 Nm at the knee and 5 Nm at the ankle during uncompensated fast walking (1.207 m/s). The peak for the knee occurs at the start of swing phase, where accelerations are highest. The peak for the ankle occurs at the initial stance primarily because of acceleration associated with the heel striking the ground. The knee torque is higher than the ankle because of the knee's higher acceleration. With closed-loop torque control, the peak backdrive torque drops to lower than 3 Nm. The mean value of the absolute torque is reduced by 22.9%

for the ankle and 63.13% for the knee. The peak backdrive torque is reduced by 57.87% for the ankle and 63.56% for the knee [34]. These backdrive torques are an order of magnitude smaller than normative human joint torques [44] and would likely be even smaller in a clinical application, where slower walking speeds are expected. Improved alignment of the exoskeleton brace with the anatomical joint axes of rotation could further reduce the backdrive torques.

### *Underactuated Potential Energy Shaping for a Unilateral Exoskeleton*

Gait rehabilitation after a stroke often involves locomotor training, while a fraction of the patient's body weight is offloaded by a harness [79]. This inspires the implementation of PE shaping on the unilateral powered knee-ankle exoskeleton to provide BWS on the affected side. This part reports the implementation and preliminary experiments with an able-bodied human subject.

#### Controller Implementation

To implement the PE-shaping controller, we first set  $M_\lambda = \tilde{M}_\lambda$  in (41), that is, not shaping the KE. Because we are interested

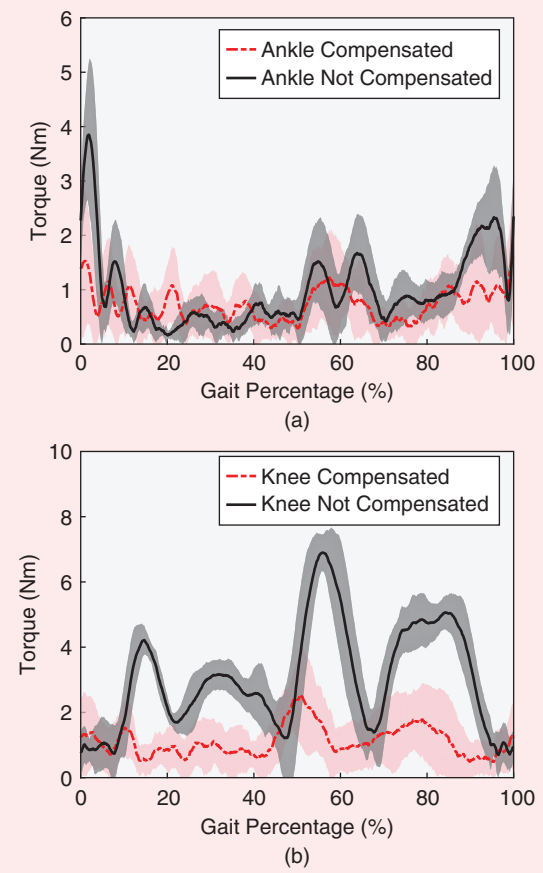


**FIGURE 16** The measured backdrive torque during passive walking: average absolute values and error bars ( $\pm 1$  standard deviation shown in shaded regions) of ten steady steps. (Figure reproduced from [34].)

**TABLE 5 Model parameters for the potential energy-shaping controller implemented on the knee-ankle exoskeleton for human subject experiments. The segment masses of the subject were calculated based on [44]. The lengths of the subject's limbs and the exoskeleton masses were measured. The exoskeleton and human masses were combined in the control law calculation to provide weight support for both the human and exoskeleton.**

Parameter	Variable	Value
Hip and upper body mass	$m_h$	54.835 kg
Thigh mass	$m_t$	11.228 kg
Shank mass	$m_s$	6.582 kg
Foot mass	$m_f$	1.745 kg
Knee exoskeleton mass	$m_k$	2.106 kg
Ankle exoskeleton mass	$m_a$	1.843 kg
Shoe insert mass	$m_{sh}$	0.356 kg
Shank length	$l_s$	0.41 m
Thigh length	$l_t$	0.44 m
Foot length	$l_f$	0.2736 m

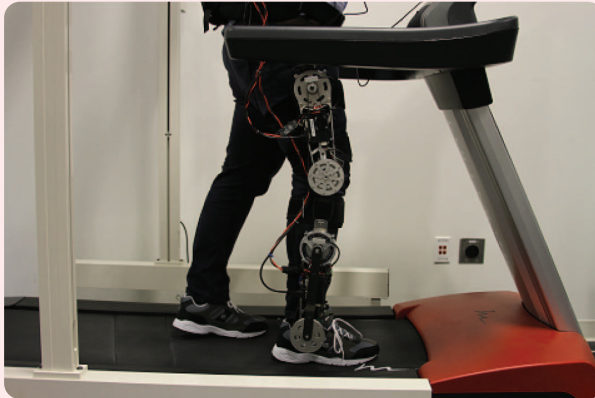
in controlling a unilateral knee-ankle exoskeleton using only feedback local to its leg, the dynamical models of the stance and swing legs are separated for the purpose of control derivation. The configuration vectors for both the stance and swing models are given as

$$q_{st} = (p_x, p_y, \phi, \theta_a, \theta_k)^T \in \mathbb{R}^5, \quad q_{sw} = (h_x, h_y, \theta_{th}, \theta_{sk}, \theta_{sa})^T \in \mathbb{R}^5.$$

The subscripts st and sw indicate stance and swing, and the stance leg configuration  $q_{st}$  is defined similar to the full biped model configuration vector  $q$ . The hip is chosen as a floating base for the swing leg's kinematic chain, where  $(h_x, h_y)^T$  are the Cartesian positions of the hip, and  $\theta_{th}$  is the absolute angle from the vertical axis to the swing thigh. Derivations in [36] demonstrate that the proposed matching framework yields a uniform stance control law  $u_{st}$  (equivalent across stance contact conditions) and swing control law  $u_{sw}$  as

$$u_{st} = (1 - \mu)N_{st(4,5)}, \quad u_{sw} = (1 - \mu)N_{sw(4,5)}. \quad (47)$$

These control laws only require position feedback, where joint angles are measured by joint encoders and global



(a)



(b)



(c)

**FIGURE 17** Photos of multiple task experiments. (a) The treadmill test, (b) the sit-to-stand-to-sit test, (c) and the stair ascent/descent tests.

orientation is measured by the IMU. Moreover, the control laws do not prescribe joint kinematics and thus are able to provide task-invariant assistance. Instead of recognizing the user's intention to switch between numerous controllers in a finite-state machine [13], [80]–[82], the control law (47) switches only between stance and swing. The model parameters used in these two control laws are given in Table 5. The following experiments with PE shaping did not utilize the outer torque loop in Figure 8 because the previously reported dynamic backdrive torques were acceptably small without active torque compensation (and it would be desirable to remove expensive torque sensors in future designs).

### Treadmill Walking Test

The first experimental task with PE shaping was walking on a treadmill [Figure 17(a)]. A safety harness was used to prevent potential falls. Before recording data, the subject was given time to acclimate to the unpowered exoskeleton and find a natural walking gait. Then, the subject was asked to stand straight while the exoskeleton's sensors were initialized. After activating the controller with positive or

negative BWS, the subject started walking on the treadmill at a constant speed of 0.894 m/s. Data was recorded for 12 strides after the subject achieved a steady gait.

During the positive BWS walking test, the exoskeleton applied 10% BWS during stance and 20% BWS during swing. A larger BWS ratio was used during the swing phase to increase the torque amplitude. Figure 18(a) and (b) shows the commanded and measured torques (averaged over 12 strides) in comparison to the normative human joint torques [44] scaled by the BWS ratio. The ankle actuator generated positive (dorsiflexion) torque during early stance and negative (plantarflexion) torque during late stance to help the subject with weight acceptance and push off, respectively. The knee actuator generated positive (extension) torque during most of stance to offload body weight from the subject's knee joint. The subject reported feeling assistance and was able to walk comfortably.

The second test added virtual weight to the subject with -5% BWS during stance and -10% BWS during swing. The resulting torques are shown in Figure 18(c) and (d). Instead of assisting the subject, both the knee and ankle actuators generated flexion torques during stance to prevent the subject from

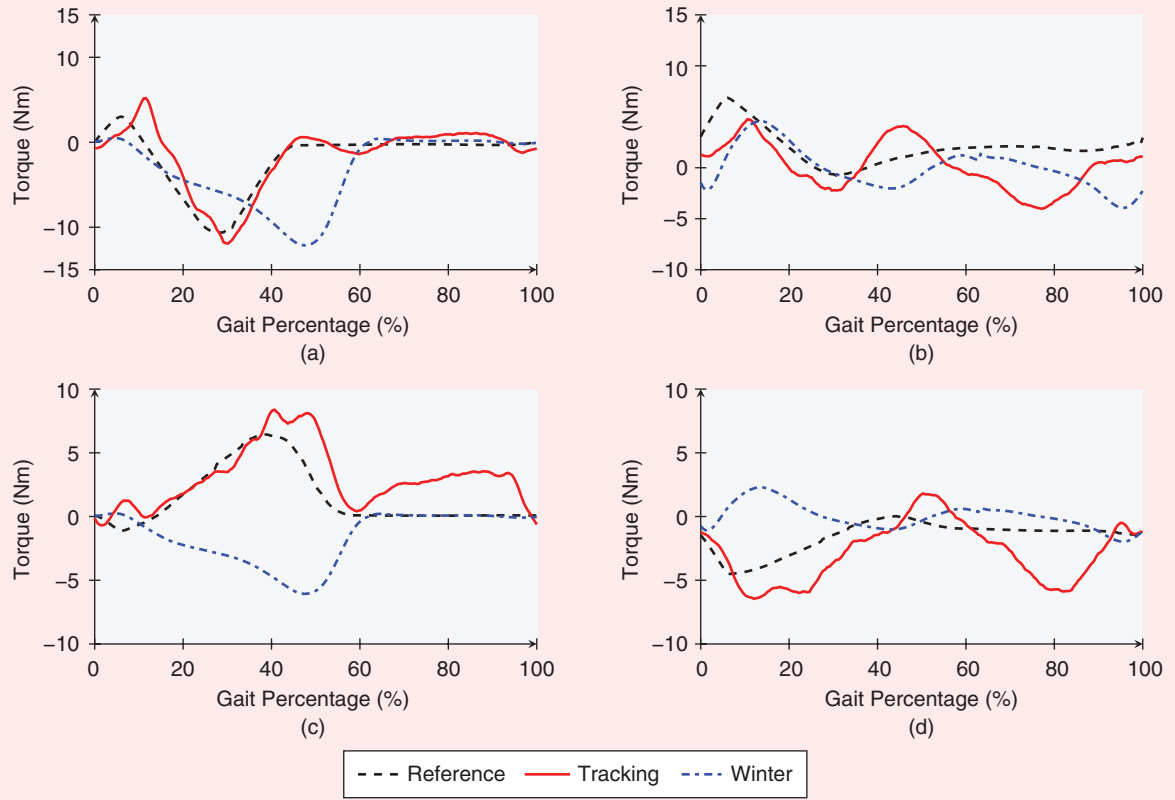


**FIGURE 18** The measured torque from walking tests (averaged over 12 strides). For the knee torque, positive indicates extension while negative indicates flexion. For the ankle torque, positive indicates dorsiflexion while negative indicates plantarflexion. For the positive body-weight support (BWS) walking test, the BWS ratio is set to  $(BWS_{st}, BWS_{sw}) = (10\%, 20\%)$ , whereas the negative BWS walking test had  $(BWS_{st}, BWS_{sw}) = (-5\%, -10\%)$ . Winter's able-bodied torque is obtained by multiplying the normalized torque data from [44] with the subject mass and BWS ratio. (a) Positive BWS walking: ankle torque, (b) positive BWS walking: knee torque, (c) negative BWS walking: ankle torque, and (d) negative BWS walking: knee torque.

extending his joints. The subject reported having to expend more effort to continue walking at 0.894 m/s under the added virtual weight. In this test, the signs of the actuator torques tended to be the opposite of the able-bodied references (providing resistance), whereas the signs tended to be aligned during the positive BWS test (providing assistance). In both cases, the torque outputs tracked the reference torques reasonably well during the stance period but not as well during the faster motions of the swing period, where the actuator's reflected inertia has more influence. This could be addressed in the future by utilizing the outer torque loop or further reducing the transmission ratio, as discussed later.

### Sit-to-Stand-to-Sit Test

To study the effects of the energy-shaping controller during sit-stand transitions, the subject was asked to stand up from a sitting posture and then immediately sit back down [Figure 17(b)]. This cycle was repeated five times with a 1–2-s break each time. The safety harness could not be used in the sitting posture; so the BWS ratio was set to 5%, and negative BWS tests were not attempted to minimize the risk of falling. Figure 19(a) and (b) shows that both the knee and ankle actuators provided extension torques to offload the user's body weight while standing up and sitting down. As a consequence, the standing motion was accelerated while the sitting motion was slowed, so the standing motion accounts for only 35% of the cycle. The subject reported feeling that the sit-to-stand cycle was easier with the assistance.

### Stair-Climbing Test

The stair-climbing test [Figure 17(c)] was performed on an indoor staircase with handrails. We began data recording from the first step until the subject reached the end of the stairs (a total of seven steps). Once the subject finished climbing, he was asked to turn around and walk downstairs. For safety reasons, the subject was only provided with 10% BWS going up and down the stairs, and negative BWS was not attempted. The recorded data for upstairs and downstairs are shown in Figure 19(c)–(f). The ankle actuator provided plantarflexion torque, and the knee actuator provided extension torque during stance to offload body weight, reducing the user's effort to propel his COM up the stairs or decelerate his COM during stair descent. The subject was able to walk stably and reported feeling comfortable and confident during both locomotor tasks without holding the handrail.

### LIMITATIONS AND FUTURE RESEARCH

Although these simulation and experimental results demonstrate the potential of the proposed design and control philosophy, some limitations still remain to be overcome. First and foremost, KE shaping needs to be implemented in hardware. The control law (41) depends on  $M_\lambda$  and  $\tilde{M}_\lambda$ , which include mass/inertia parameters of the exoskeleton and human limbs. The exoskeleton

parameters can be estimated using standard system-identification methods [5], and human parameters can be estimated from the user's weight and limb lengths based on formulas from cadaver studies [70]. Parametric errors will result in slightly different closed-loop system parameters than anticipated, but the overall effect of inertia and/or weight compensation will still be achieved. In other words, the actuator torques will still provide assistance/resistance but will be in different magnitudes due to parameter uncertainties.

Future work for control design includes shaping not only the limb inertias but also the mass terms in the inertia matrix. The main challenge is to ensure the positive definiteness of the shaped mass/inertia matrix so the control law remains well defined. Future work could also attempt to avoid the algebraic simplifications used to solve the matching conditions (that is, shaping only the actuated coordinates), which could provide more effective shaping strategies for human assistance. Ultimately, we will investigate how the choice of  $\tilde{M}$  promotes different gait characteristics in both able-bodied human subjects and poststroke individuals.

Although the powered knee-ankle exoskeleton provided adequate backdrivability and torque density, significant improvements can still be made. It would be desirable to further reduce the dynamic backdrive torque and improve torque tracking (without a torque sensor) through the use of an even lower transmission ratio. The presented prototype is also cumbersome to don and doff for the user. Therefore, ongoing work includes the design and testing of our next-generation powered knee orthosis [Generation Two, Figure 1(c)]. This device has a custom PMSM motor with greater torque density to allow the use of a 7:1 one-stage planetary gearbox, which has approximately 1/10 the reflected inertia of the generation one actuator. This design aims to assist elderly individuals and enhance the capabilities of fully able-bodied users, and it will be tested in both unilateral and bilateral configurations depending on user needs.

### CONCLUSION

In this article, we summarized past and ongoing work to present the design and control philosophy for highly backdrivable lower-limb exoskeletons. By combining torque-dense electrical motors and low-ratio custom transmissions, high-torque output and intrinsic backdrivability were achieved simultaneously with minimal production cost. To provide human-cooperative exoskeletal assistance, we proposed a complete theoretical framework for underactuated total energy shaping that incorporates both environmental and human interaction. This general matching framework yields task-invariant, trajectory-free control laws that can accommodate different activities of daily living. Next, we simulated different energy-shaping strategies on a human-like 8DOF biped to study their possible effects and benefits for human assistance. Finally, we implemented the PE-shaping strategy on the designed knee-ankle exoskeleton

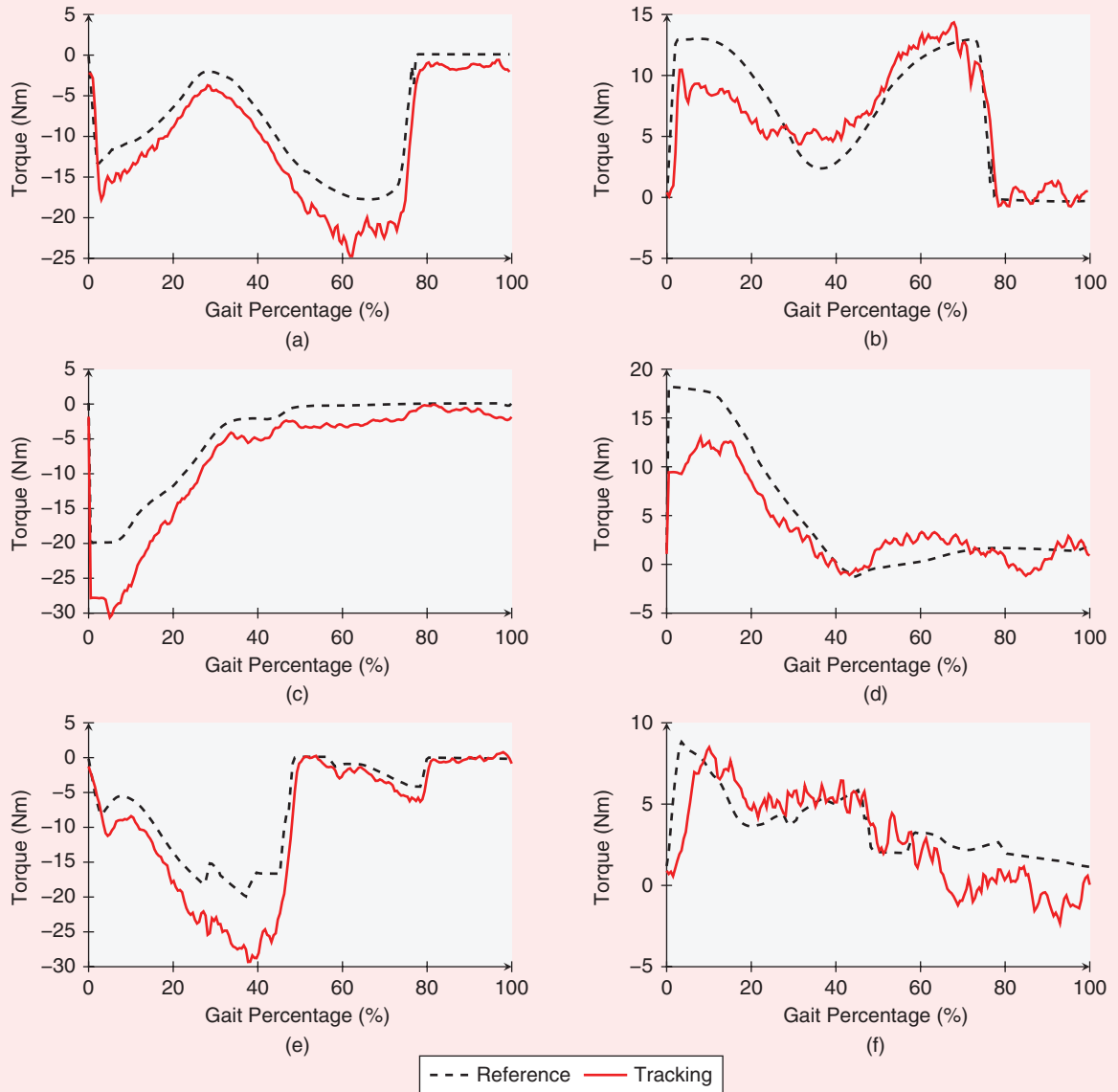


**FIGURE 19** The measured torque from the sit-to-stand-to-sit test (averaged over five cycles) and the stair ascent/descent tests (each averaged over seven strides). The direction of torques aligns with the ones in Figure 18(a)–(d). For the sit-to-stand-to-sit test, the body-weight support (BWS) ratio was set to 5%. For both stair ascent and descent tests, the BWS ratio was set to 10% for both the stance and swing controllers. (a) Sit-to-stand-to-sit: ankle torque, (b) sit-to-stand-to-sit: knee torque, (c) stair ascent: ankle torque, (d) stair ascent: knee torque, (e) stair descent: ankle torque, and (f) stair descent: knee torque.

and conducted experiments with an able-bodied subject. The subject was free to move his joints with minimal resistance from the exoskeleton actuators, and the PE-shaping controller provided the subject with consistent assistance during positive BWS tests or resistance during negative BWS tests. Future work will further refine this design/control philosophy and study clinical outcomes for different patient populations.

## ACKNOWLEDGMENTS

This work was supported by the National Institute of Child Health and Human Development of the National Institutes

of Health (NIH) under Award Number DP2HD080349. This work was also supported by National Science Foundation (NSF) Award CMMI-1652514. The content is solely the responsibility of the authors and does not necessarily represent the official views of the NIH or the NSF. Robert D. Gregg holds a Career Award at the Scientific Interface from the Burroughs Wellcome Fund.

## AUTHOR INFORMATION

*Ge Lv* received the B.S. and the M.S. degrees in information science and engineering from Northeastern University, Shenyang, China, in 2011 and 2013, respectively. He joined

the Department of Electrical Engineering at The University of Texas at Dallas as a Ph.D. student in 2013. His research is in the control of bipedal locomotion with applications to orthoses and exoskeletons. He received the Best Student Paper Award of the 2015 IEEE Conference on Decision and Control.

**Hanqi Zhu** received the B.S. and the M.S. degrees in mechanical engineering from the Xi'an Jiaotong University, China, in 2011 and 2013, respectively. He is pursuing a second M.S. degree and a Ph.D. degree in the Department of Electrical Engineering at The University of Texas at Dallas. His research is in the design of advanced mechatronics systems with applications to wearable rehabilitation robots.

**Robert D. Gregg** (rgregg@ieee.org) received the B.S. degree in electrical engineering and computer sciences from the University of California, Berkeley, in 2006 and the M.S. and Ph.D. degrees in electrical and computer engineering from the University of Illinois at Urbana-Champaign in 2007 and 2010, respectively. He joined the Departments of Bioengineering and Mechanical Engineering at The University of Texas at Dallas (UTD) as an assistant professor in 2013. Prior to joining UTD, he was a research scientist at the Rehabilitation Institute of Chicago, Illinois, and a postdoctoral fellow at Northwestern University, Evanston, Illinois. His research is in the control of bipedal locomotion with applications to autonomous and wearable robots. He is a Senior Member of the IEEE. He can be contacted at the University of Texas, 800 West Campbell Road, Mailstop EC-32, Richardson, Texas 75080-3021.

## REFERENCES

- [1] T. Yan, M. Cempini, C. M. Oddo, and N. Vitiello, "Review of assistive strategies in powered lower-limb orthoses and exoskeletons," *Robot. Autonomous Syst.*, vol. 64, pp. 120–136, Feb. 2015.
- [2] G. Zeilig, H. Weingarten, M. Zwecker, I. Dudkiewicz, A. Bloch, and A. Esquenazi, "Safety and tolerance of the rewalk™ exoskeleton suit for ambulation by people with complete spinal cord injury: A pilot study," *J. Spinal Cord Med.*, vol. 35, no. 2, pp. 96–101, 2012.
- [3] S. A. Kolakowsky-Hayner, J. Crew, S. Moran, and A. Shah, "Safety and feasibility of using the Ekso Bionics exoskeleton to aid ambulation after spinal cord injury," *J. Spine*, vol. 4, p. 003, 2013. doi:10.4172/2165-7939.S4-003.
- [4] A. Agrawal, O. Harib, A. Hereid, S. Finet, M. Masselin, L. Praly, A. D. Ames, K. Sreenath, and J. W. Grizzle, "First steps towards translating H2D control of bipedal robots to decentralized control of exoskeletons," *IEEE Access*, vol. 5, pp. 9919–9934, Apr. 2017.
- [5] J. Ghan, R. Steger, and H. Kazerooni, "Control and system identification for the Berkeley Lower Extremity Exoskeleton (BLEEX)," *Adv. Robot.*, vol. 20, no. 9, pp. 989–1014, 2006.
- [6] B. Quinlivan, S. Lee, P. Malcolm, D. Rossi, M. Grimmer, C. Siviy, N. Karavas, D. Wagner, A. Asbeck, I. Galiana, and C. J. Walsh, "Assistance magnitude versus metabolic cost reductions for a tethered multiarticular soft exosuit," *Sci. Robot.*, vol. 2, no. 2, pp. 4416–4416, 2017.
- [7] J. E. Pratt, B. T. Krupp, C. J. Morse, and S. H. Collins, "The roboknee: An exoskeleton for enhancing strength and endurance during walking," in *Proc. IEEE Int. Conf. Robotics and Automation*, vol. 3, pp. 2430–2435, 2004.
- [8] J. A. Blaya and H. Herr, "Adaptive control of a variable-impedance ankle-foot orthosis to assist drop-foot gait," *IEEE Trans. Neural Syst. Rehabil. Eng.*, vol. 12, no. 1, pp. 24–31, 2004.
- [9] H. Kawamoto and Y. Sankai, "Power assist system HAL-3 for gait disorder person," in *Proc. Int. Conf. Computers for Handicapped Persons*, 2002, pp. 196–203.
- [10] H. Aguilar-Sierra, R. Lopez, W. Yu, S. Salazar, and R. Lozano, "A lower limb exoskeleton with hybrid actuation," in *Proc. IEEE Int. Conf. Biomedical Robotics and Biomechatronics*, 2014, pp. 695–700.
- [11] R. Lu, Z. Li, C.-Y. Su, and A. Xue, "Development and learning control of a human limb with a rehabilitation exoskeleton," *IEEE Trans. Ind. Electron.*, vol. 61, no. 7, pp. 3776–3785, 2014.
- [12] K. Kiguchi and Y. Yokomine, "Walking assist for a stroke survivor with a power-assist exoskeleton," in *Proc. IEEE Int. Conf. Systems, Man and Cybernetics*, 2014, pp. 1888–1892.
- [13] S. A. Murray, K. H. Ha, C. Hartigan, and M. Goldfarb, "An assistive control approach for a lower-limb exoskeleton to facilitate recovery of walking following stroke," *IEEE Trans. Neural Syst. Rehabil. Eng.*, vol. 23, no. 3, pp. 441–449, 2015.
- [14] R. Jimenez-Fabian and O. Verlinden, "Review of control algorithms for robotic ankle systems in lower-limb orthoses, prostheses, and exoskeletons," *Med. Eng. Phys.*, vol. 34, no. 4, pp. 397–408, 2012.
- [15] R. D. Gregg, T. Lenzi, L. J. Hargrove, and J. W. Sensinger, "Virtual constraint control of a powered prosthetic leg: From simulation to experiments with transfemoral amputees," *IEEE Trans. Robot.*, vol. 30, no. 6, pp. 1455–1471, Dec. 2014.
- [16] D. Quintero, D. J. Villarreal, D. J. Lambert, S. Kapp, and R. D. Gregg, "Continuous-phase control of a powered knee–ankle prosthesis: Amputee experiments across speeds and inclines," *IEEE Trans. Robot.*, vol. 34, no. 3, pp. 686–701, June 2018.
- [17] A. Duschau-Wicke, T. Brunsch, L. Lunenburger, and R. Riener, "Adaptive support for patient-cooperative gait rehabilitation with the Lokomat," in *Proc. IEEE/RSJ Int. Conf. Intelligent Robots and Systems*, 2008, pp. 2357–2361.
- [18] S. Seok, A. Wang, M. Y. M. Chuah, D. J. Hyun, J. Lee, D. M. Otten, J. H. Lang, and S. Kim, "Design principles for energy-efficient legged locomotion and implementation on the MIT Cheetah robot," *IEEE/ASME Trans. Mechatrons*, vol. 20, no. 3, pp. 1117–1129, 2015.
- [19] H.-W. Park, P. M. Wensing, and S. Kim, "High-speed bounding with the MIT Cheetah 2: Control design and experiments," *Int. J. Robot. Res.*, vol. 36, no. 2, pp. 167–192, 2017.
- [20] R. Ferris, H. Quintero, and M. Goldfarb, "Preliminary evaluation of a powered lower limb orthosis to aid walking in paraplegic individuals," *IEEE Trans. Neural Syst. Rehabil. Eng.*, vol. 19, no. 6, pp. 652–659, 2011.
- [21] H. Kaminaga, T. Amari, Y. Niwa, and Y. Nakamura, "Development of knee power assist using backdrivable electro-hydrostatic actuator," in *Proc. IEEE Int. Conf. Intelligent Robots and Systems*, 2010, pp. 5517–5524.
- [22] P. A. Bhounsule, J. Cortell, A. Grewal, B. Hendriksen, J. D. Karssen, C. Paul, and A. Ruina, "Low-bandwidth reflex-based control for lower power walking: 65 km on a single battery charge," *Int. J. Robot. Res.*, vol. 33, no. 10, pp. 1305–1321, 2014.
- [23] K. Kong, J. Bae, and M. Tomizuka, "Control of rotary series elastic actuator for ideal force-mode actuation in human–robot interaction applications," *IEEE/ASME Trans. Mechatrons*, vol. 14, no. 1, pp. 105–118, 2009.
- [24] K. Kong, J. Bae, and M. Tomizuka, "A compact rotary series elastic actuator for human assistive systems," *IEEE/ASME Trans. Mechatrons*, vol. 17, no. 2, pp. 288–297, 2012.
- [25] H. Yu, M. Sta Cruz, G. Chen, S. Huang, C. Zhu, E. Chew, Y. S. Ng, and N. V. Thakor, "Mechanical design of a portable knee–ankle–foot robot," in *Proc. IEEE Int. Conf. Robotics and Automation*, 2013, pp. 2183–2188.
- [26] B. Brackx, J. Geeroms, J. Vantilt, V. Grosu, K. Junius, H. Cuypers, B. Vanderborght, and D. Lefebre, "Design of a modular add-on compliant actuator to convert an orthosis into an assistive exoskeleton," in *Proc. IEEE Int. Conf. Biomedical Robotics and Biomechatronics*, 2014, pp. 485–490.
- [27] D. W. Robinson, "Design and analysis of series elasticity in closed-loop actuator force control," Ph.D. dissertation, Massachusetts Inst. Tech., Cambridge, MA, 2000.
- [28] A. T. Asbeck, S. M. De Rossi, K. G. Holt, and C. J. Walsh, "A biologically inspired soft exosuit for walking assistance," *Int. J. Robot. Res.*, vol. 34, no. 6, pp. 744–762, 2015.
- [29] G. Kenneally, A. De, and D. E. Koditschek, "Design principles for a family of direct-drive legged robots," *IEEE Robot. Autom. Lett.*, vol. 1, no. 2, pp. 900–907, 2016.
- [30] U. Nagarajan, G. Aguirre-Ollinger, and A. Goswami, "Integral admittance shaping: A unified framework for active exoskeleton control," *Robot. Autonomous Syst.*, vol. 75, pp. 310–324, 2016.
- [31] G. Aguirre-Ollinger, J. E. Colgate, M. A. Peshkin, and A. Goswami, "Inertia compensation control of a one-degree-of-freedom exoskeleton for lower-limb assistance: Initial experiments," *IEEE Trans. Neural Syst. Rehabil. Eng.*, vol. 20, no. 1, pp. 68–77, 2012.
- [32] J. K. Holm and M. W. Spong, "Kinetic energy shaping for gait regulation of underactuated bipeds," in *Proc. IEEE Int. Conf. Control Applications*, pp. 1232–1238, 2008.

- [33] G. Lv, H. Zhu, T. Elery, L. Li, and R. D. Gregg, "Experimental implementation of underactuated potential energy shaping on a powered ankle-foot orthosis," in *Proc. IEEE Int. Conf. Robotics and Automation*, 2016, pp. 3493–3500.
- [34] H. Zhu, J. Doan, C. Stence, G. Lv, T. Elery, and R. Gregg, "Design and validation of a torque dense, highly backdrivable powered knee-ankle orthosis," in *Proc. IEEE Int. Conf. Robotics and Automation*, May 2017, pp. 504–510.
- [35] G. Lv and R. D. Gregg, "Orthotic body-weight support through underactuated potential energy shaping with contact constraints," in *Proc. IEEE 54th Conf. Decision and Control*, 2015, pp. 1483–1490.
- [36] G. Lv and R. D. Gregg, "Underactuated potential energy shaping with contact constraints: Application to a powered knee-ankle orthosis," *IEEE Trans. Control Syst. Technol.*, vol. 26, no. 1, pp. 181–193, 2018.
- [37] G. Lv and R. D. Gregg, "Towards total energy shaping control of lower-limb exoskeletons," in *Proc. IEEE American Control Conf.*, 2017, pp. 4851–4857.
- [38] T. Elery, S. Rezazadeh, C. Nesler, J. Doan, H. Zhu, and R. Gregg, "Design and benchtop validation of a powered knee-ankle prosthesis with high-torque, low-impedance actuators," in *Proc. IEEE Int. Conf. Robotics and Automation*, 2018, pp. 2788–2795.
- [39] R. L. Waters and S. Mulroy, "The energy expenditure of normal and pathologic gait," *Gait Posture*, vol. 9, no. 3, pp. 207–231, 1999.
- [40] J. M. del Castillo, "The analytical expression of the efficiency of planetary gear trains," *Mechanism Mach. Theory*, vol. 37, no. 2, pp. 197–214, 2002.
- [41] R. Krishnan, *Permanent Magnet Synchronous and Brushless DC Motor Drives*. Boca Raton, FL: CRC Press, 2009.
- [42] M. E. Dohring, E. Lee, and W. S. Newman, "A load-dependent transmission friction model: Theory and experiments," in *Proc. IEEE Int. Conf. Robotics and Automation*, 1993, pp. 430–436.
- [43] J. W. Sensinger, "Efficiency of high-sensitivity gear trains, such as cycloid drives," *ASME J. Mech. Design*, vol. 135, no. 7, p. 071006, 2013.
- [44] D. A. Winter, *Biomechanics and Motor Control of Human Movement*, 2nd ed. Hoboken, NJ: Wiley, 2009.
- [45] A. J. Young and D. P. Ferris, "State of the art and future directions for lower limb robotic exoskeletons," *IEEE Trans. Neural Syst. Rehabil. Eng.*, vol. 25, no. 2, pp. 171–182, 2017.
- [46] A. Goswami, B. Thuilot, and B. Espiau, "A study of the passive gait of a compass-like biped robot: Symmetry and chaos," *Int. J. Robot. Res.*, vol. 17, no. 12, pp. 1282–1301, 1998.
- [47] T. McGeer, "Passive dynamic walking," *Int. J. Robot. Res.*, vol. 9, no. 2, pp. 62–82, 1990.
- [48] R. D. Gregg, T. W. Bred, and M. W. Spong, "A control theoretic approach to robot-assisted locomotor therapy," in *Proc. IEEE Conf. Decision and Control*, pp. 1679–1686, 2010.
- [49] J. K. Holm, D. Lee, and M. W. Spong, "Time-scaling trajectories of passive-dynamic bipedal robots," in *Proc. IEEE Int. Conf. Robotics and Automation*, 2007, pp. 3603–3608.
- [50] R. Ortega, J. A. L. Perez, P. J. Nicklasson, and H. Sira-Ramirez, *Passivity-Based Control of Euler-Lagrange Systems: Mechanical, Electrical and Electromechanical Applications*. Berlin, Germany: Springer Science, 1998.
- [51] R. Ortega, A. J. Van der Schaft, I. Mareels, and B. Maschke, "Putting energy back in control," *IEEE Control Syst. Mag.*, vol. 21, no. 2, pp. 18–33, 2001.
- [52] G. Blankenstein, R. Ortega, and A. J. Van Der Schaft, "The matching conditions of controlled Lagrangians and IDA-passivity based control," *Int. J. Control.*, vol. 75, no. 9, pp. 645–665, 2002.
- [53] R. Ortega, M. W. Spong, F. Gomez-Estern, and G. Blankenstein, "Stabilization of a class of underactuated mechanical systems via interconnection and damping assignment," *IEEE Trans. Automat. Control*, vol. 47, no. 8, pp. 1218–1233, 2002.
- [54] A. M. Bloch, D. E. Chang, N. E. Leonard, and J. E. Marsden, "Controlled Lagrangians and the stabilization of mechanical systems II: Potential shaping," *IEEE Trans. Automat. Control*, vol. 46, no. 10, pp. 1556–1571, 2001.
- [55] J. Holm, "Gait regulation for robotic bipedal locomotion," Ph.D. dissertation, University of Illinois at Urbana-Champaign, 2008.
- [56] R. M. Murray, Z. Li, and S. S. Sastry, *A Mathematical Introduction to Robotic Manipulation*. Boca Raton, FL: CRC Press, 1994.
- [57] A. E. Martin, D. C. Post, and J. P. Schmideler, "Design and experimental implementation of a hybrid zero dynamics-based controller for planar bipeds with curved feet," *Int. J. Robot. Res.*, vol. 33, no. 7, pp. 988–1005, 2014.
- [58] R. D. Gregg and M. W. Spong, "Reduction-based control of three-dimensional bipedal walking robots," *Int. J. Robot. Res.*, vol. 29, no. 6, pp. 680–702, 2010.
- [59] A. Grabowski, C. T. Farley, and R. Kram, "Independent metabolic costs of supporting body weight and accelerating body mass during walking," *J. Appl. Physiol.*, vol. 98, no. 2, pp. 579–583, 2005.
- [60] F. Ghorbel, B. Srinivasan, and M. W. Spong, "On the uniform boundedness of the inertia matrix of serial robot manipulators," *J. Robot. Syst.*, vol. 15, no. 1, pp. 17–28, 1998.
- [61] D. J. Braun, J. E. Mitchell, and M. Goldfarb, "Actuated dynamic walking in a seven-link biped robot," *IEEE/ASME Trans. Mechatrons*, vol. 17, no. 1, pp. 147–156, 2012.
- [62] D. J. Braun and M. Goldfarb, "A control approach for actuated dynamic walking in biped robots," *IEEE Trans. Robot.*, vol. 25, no. 6, pp. 1292–1303, 2009.
- [63] S. Mochon and T. A. McMahon, "Ballistic walking," *J. Biomech.*, vol. 13, no. 1, pp. 49–57, 1980.
- [64] A. E. Minetti, C. Moia, G. S. Roi, D. Susta, and G. Ferretti, "Energy cost of walking and running at extreme uphill and downhill slopes," *J. Appl. Physiol.*, vol. 93, no. 3, pp. 1039–1046, 2002.
- [65] E. R. Westervelt, J. W. Grizzle, and D. E. Koditschek, "Hybrid zero dynamics of planar biped walkers," *IEEE Trans. Automat. Control*, vol. 48, no. 1, pp. 42–56, 2003.
- [66] J. Grizzle, E. Westervelt, C. Chevallereau, J. Choi, and B. Morris, *Feedback Control of Dynamic Bipedal Robot Locomotion*. Boca Raton, FL: CRC Press, 2007.
- [67] A. Goswami, B. Thuilot, and B. Espiau, "Compass-like biped robot part I: Stability and bifurcation of passive gaits," Institut National de Recherche en Informatique et en Automatique (INRIA), Grenoble, France, Tech. Rep. 2996, 1996.
- [68] R. D. Gregg, Y. Y. Dhaher, A. Degani, and K. M. Lynch, "On the mechanics of functional asymmetry in bipedal walking," *IEEE Trans. Biomed. Eng.*, vol. 59, no. 5, pp. 1310–1318, 2012.
- [69] J. B. Dingwell and H. G. Kang, "Differences between local and orbital dynamic stability during human walking," *ASME J. Biomed. Eng.*, vol. 129, no. 4, p. 586, Dec. 2006.
- [70] P. De Leva, "Adjustments to Zatsiorsky-Seluyanov's segment inertia parameters," *J. Biomed.*, vol. 29, no. 9, pp. 1223–1230, 1996.
- [71] S. L. Kilbreath, S. Perkins, J. Crosbie, and J. McConnell, "Gluteal taping improves hip extension during stance phase of walking following stroke," *Australian J. Physiotherapy*, vol. 52, no. 1, pp. 53–56, 2006.
- [72] S. H. Collins, M. B. Wiggin, and G. S. Sawicki, "Reducing the energy cost of human walking using an unpowered exoskeleton," *Nature*, vol. 522, no. 7555, pp. 212–215, 2015.
- [73] A. Silder, T. Besier, and S. L. Delp, "Predicting the metabolic cost of incline walking from muscle activity and walking mechanics," *J. Biomed.*, vol. 45, no. 10, pp. 1842–1849, 2012.
- [74] A. E. Martin and J. P. Schmideler, "Predicting human walking gaits with a simple planar model," *J. Biomed.*, vol. 47, no. 6, pp. 1416–1421, 2014.
- [75] R. Alexander, "Optimization and gaits in the locomotion of vertebrates," *Physiol. Rev.*, vol. 69, no. 4, pp. 1199–1227, 1989.
- [76] F. Saibene and A. E. Minetti, "Biomechanical and physiological aspects of legged locomotion in humans," *Eur. J. Appl. Physiol.*, vol. 88, no. 4, pp. 297–316, 2003.
- [77] F. Lacquaniti, Y. P. Ivanenko, F. Sylos Labini, V. La Scaleia, B. La Scaleia, P. A. Willems, and M. Zago, "Human locomotion in hypogravity: From basic research to clinical applications," *Front. Physiol.*, vol. 8, p. 893, Nov. 2017.
- [78] S. J. Olney and C. Richards, "Hemiparetic gait following stroke. Part I: Characteristics," *Gait Posture*, vol. 4, no. 2, pp. 136–148, 1996.
- [79] M. Franceschini, S. Carda, M. Agosti, R. Antenucci, D. Malgrati, and C. Cisari, "Walking after stroke: What does treadmill training with body weight support add to overground gait training in patients early after stroke? A single-blind, randomized, controlled trial," *Stroke*, vol. 40, no. 9, pp. 3079–3085, 2009.
- [80] A. Tsukahara, Y. Hasegawa, and Y. Sankai, "Gait support for complete spinal cord injury patient by synchronized leg-swing with HAL," in *Proc. IEEE/RSJ 2011 Int. Conf. Intelligent Robots and Systems*, 2011, pp. 1737–1742.
- [81] T. Yan, A. Parri, M. Fantozzi, M. Cortese, M. Muscolo, M. Cempini, F. Giovacchini, G. Pasquini, M. Munih, and N. Vitiello, "A novel adaptive oscillators-based control for a powered multi-joint lower-limb orthosis," in *Proc. IEEE 2015 Int. Conf. Rehabilitation Robotics*, 2015, pp. 386–391.
- [82] V. R. Garate, A. Parri, T. Yan, M. Munih, R. M. Lova, N. Vitiello, and R. Ronse, "Experimental validation of motor primitive-based control for leg exoskeletons during continuous multi-locomotion tasks," *Front. Neurosci.*, vol. 11, Mar. 2017, doi: 10.3389/fnbot.2017.00015.